Laser Thermal Processing of Group IV Semiconductors for Integrated Photonic Systems

Ozan Aktas and Anna C. Peacock**

Dr. O. Aktas, Prof. A. C. Peacock
Optoelectronics Research Centre,
University of Southampton,
Southampton, SO17 1BJ, UK
E-mail: acp@orc.soton.ac.uk;

Keywords: laser processing, group IV semiconductors, integrated photonics, semiconductor core glass-clad fibers, planar photonic devices, silicon-germanium, germanium-tin

Abstract

In the quest to expand the functionality and capacity of group IV semiconductor photonic systems, new materials and production methods are constantly being explored. In particular, flexible fabrication and post-processing approaches that are compatible with different materials and allow for tuning of the components and systems are of great interest. Within this research area, laser thermal processing has emerged as an indispensable tool that can be applied to enhance and/or modify the material, structural, electrical and optical properties of group IV elemental and compound semiconductors at various stages of the production process. This review evaluates the recent progress made in the application of laser processing techniques to develop integrated semiconductor systems in both fiber and planar-based platforms. Laser processing has allowed for the production of semiconductor waveguides with high crystallinity in the core and low optical losses, as well as post-fabrication trimming of device characteristics and direct writing of tunable strain and composition profiles for bandgap engineering and optical waveguiding. For each platform, the current challenges and opportunities for the future development of laser-processed integrated semiconductor photonic systems are presented.

1. Introduction

Over the past two decades, remarkable progress has been made in the development of group IV semiconductor waveguide components for photonics applications.[1-4] Most of this work has focused on the development of planar integrated circuits and, in particular, on devices constructed from silicon-on-insulator (SOI) platforms.[5] The dominance of SOI platforms has been driven by the high yields and compact photonic components that are achievable from leveraging the standard microelectronics foundry processes.[6] However, despite these efforts, there are still considerable challenges to integrating photonic devices produced in this platform, both in terms of merging them with electronic components, which are predominantly built on bulk silicon (Si) wafers, and optical fiber components used for the interconnection of systems. Moreover, as a photonic material, Si suffers from some limitations, such as its indirect electronic bandgap and lack of a second order susceptibility $\chi^{(2)}$. Therefore, high performing systems can benefit from its properties being modified,[7] and/or integration with components produced from other group IV semiconductor materials such as germanium (Ge) and tin (Sn).[8,9] Certainly, there is a great need to develop more flexible production methods that allow for the integration of high quality components produced from various group IV materials, which can be adapted to achieve the required functionality within different architectures.

In this regard, group-IV semiconductors that can be produced via non-epitaxial growth methods have gained much attention over the past decade. These materials are typically produced in either amorphous or polycrystalline phases, and are compatible with both fiber and planar geometries. For example, polycrystalline silicon (poly-Si) has been exploited in both geometries for the construction of passive photonic devices, and has also been used to develop active devices and gate electrodes in planar electronic circuits, which represents an important step towards the convergence of electronics and photonics.[10] However, although these materials have clear advantages in terms of cost and flexibility in the way the components can be fabricated and integrated, the reduced quality of the material compared to the single

crystalline form limits the overall optical and electronic performance.[11] As a result, various post-processing methods have been developed based on thermal treatments to anneal these materials with the goal to enhancing device performance as well as improving fabrication yields.[12]

Perhaps the most commonly employed thermal treatment is furnace annealing, but this approach requires the entire sample to be heated to very high temperatures, which can alter or damage any integrated components, especially those with electrical connections. More recently there has been growing interest in laser processing procedures as these offer a more directed source of energy, and thus can be used to process individual components, or even parts of components, with extreme precision. In particular, the morphology of the heat zone can be manipulated by adjusting the wavelength, polarization, optical power, scan speed, micron-scale spot size and shape of the laser beam,[13] allowing for control over the heating and cooling dynamics across the sample that is not possible using more conventional heat sources. The key laser processing parameters need to be chosen and optimized depending on the material, photonic platform, and application of interest. An introduction to light-matter interactions and general guidelines for laser processing of photonic structures can be found in Ref.[14]. Although laser thermal annealing was initially conceived to remove defects in the crystal structure caused by ion-implantation,[15] the current scope and impact of laser processing is much broader and far-reaching.[16] This has been aided by the increased availability of powerful and versatile laser sources, such as CO_2 gas lasers emitting at 10.6 μm, argon-ion continuous wave (CW) lasers emitting at 488 nm, pulsed ultraviolet (UV) excimer lasers, Nd:YAG solid state lasers emitting at 1064 nm, or their second harmonic 532 nm, to name but a few. Drawing on this excellent tool box, laser thermal processing, as schematically shown in **Figure 1**, can be applied to modify and enhance the structural, thermal, electrical and optical properties of the full range of group IV semiconductors, thus opening a route to the construction of high performance integrated systems.

In this review, we focus on laser processing of group IV elemental and compound semiconductors via thermal treatments induced by the optical absorption of both CW and pulsed laser radiation. Specifically, we cover work that has been conducted in both fiber and planar photonic platforms as much can be learned from comparing and contrasting the efforts in the respective areas. We begin by presenting an overview of laser processing in the semiconductor core glass-clad fibers, where significant progress has been made to improve and modify the optical properties of the core via annealing, directional solidification, crystallization, as well as engineering of strain, bandgap, composition, structure and morphology. This is then followed by a discussion of some of the key applications of laser processing on planar photonic systems, including crystallization and trimming of waveguide components, composition engineering in semiconductor alloys, laser-assisted diffusion and alloying for selective area growth, and direct writing of semiconductor nanostructures. As well as highlighting the important advances made in the application of laser treatments, this review also identifies technological challenges and areas for future work, helping to set the scene for the wide spread adoption of laser-processed group IV semiconductors across both fiber and planar integrated photonic systems.

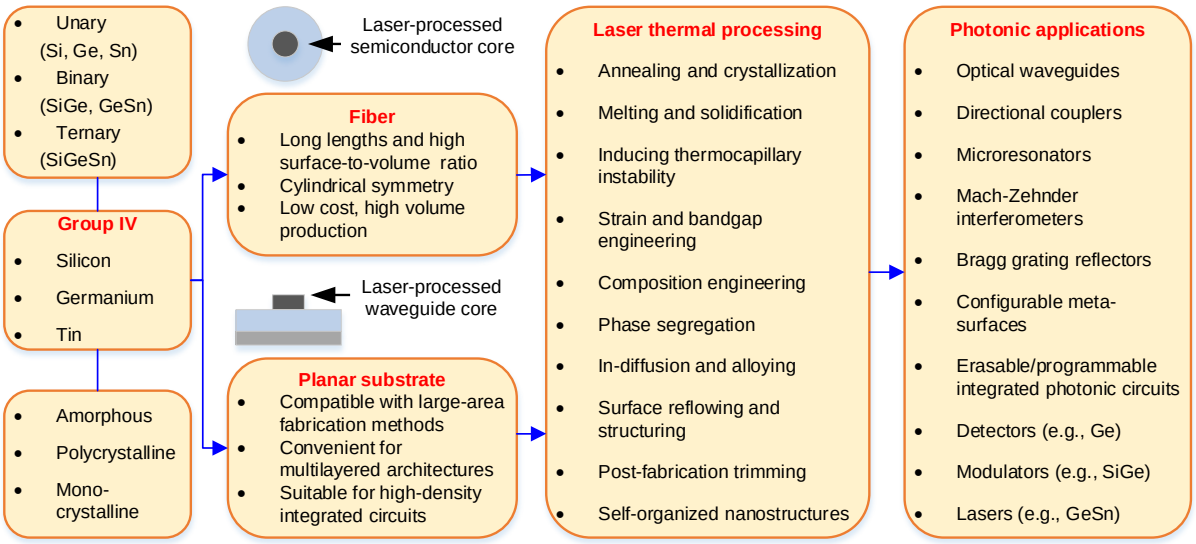

Figure 1. Schematic showing the process flow starting from growth of the group IV semiconductor materials, followed by laser thermal treatment to modify or enhance the material and/or structural properties of the components for various target applications. The processes can be adapted for both fiber and planar systems.

2. Laser-processed fiber-based photonic devices

The idea of incorporating group IV semiconductors within the cores of glass-clad fibers is quite appealing, as it is possible to turn a passive light conduit into an active medium where the electronic and/or nonlinear optical properties of the semiconductors can be leveraged to modulate or detect light within the fiber geometry. Moreover, these semiconductor fibers support integration with other fiber-based components, such as fiber laser pump sources, opening a route to producing a wide range of robust and efficient systems for applications in nonlinear optics[17], all-optical signal processing,[18] and optoelectronics.[19]. As well as elemental Si,[20] Ge[21] and Sn[22] core materials, compound semiconductor core fibers such as SiGe[23] and SnSe[24] have also been fabricated, highlighting the versatility of the production processes. However, post-process thermal treatments are generally required to enhance the material and optical qualities of as-fabricated semiconductor core fibers. Of the various post-fabrication methods developed to date, [25] which includes furnace annealing, photo-thermal annealing, etc., the most promising approach is laser thermal processing as this can not only be applied to improve the transmission properties via annealing, crystallization, and homogenization of the core, but it can also be used to engineer the bandgap, composition, refractive index, structure and even morphology. We start this section by first outlining the various fabrication methods for semiconductor core fibers before showcasing some of the most important applications of laser processing.

2.1 Fabrication of semiconductor core glass-clad fibers

There have been two primary methods developed to date for the fabrication of semiconductor core glass-clad fibers.[26,27] The first is the high pressure chemical vapor deposition (HPCVD) method,[28] which deposits semiconductors within the pore of a silica capillary by thermal decomposition of a pressurized mixture of precursor and carrier gases during their flow through the heated capillary. Deposition of Si via HPCVD is schematically shown in **Figure 2a**, where SiH_4 and He are used as a precursor and a carrier gas, respectively. Deposition of the

semiconductor is continued until a desired shell thickness or full enclosure of the pore is achieved. The carrier gas and byproducts for this reaction are sufficiently small that they eventually diffuse out through the capillary wall. Typical sizes of capillary pores that can be filled via the HPCVD method range between hundreds of nanometers to several tens of micrometers. Optical microscope images (Figure 2b) show the cross-section of a silica capillary before and after the core was filled with Si.[29] By choosing different precursors and adjusting the pressure, a variety of core materials can be deposited, including both elemental and compound semiconductors.[30] Moreover, by controlling the decomposition temperature, it is possible to tune the deposition to achieve both amorphous and crystalline phases.[31] However, perhaps the biggest advantage of this technique is the ability to deposit concentric homo and heterojunctions within the capillary pore by switching the precursor during the process, and/or via in situ doping if necessary. The major drawback of this approach is that it can take a couple of weeks for some materials to produce fibers of only a few centimeters in length. Moreover, when depositing the core materials in a crystalline form, due to difficulties in controlling the crystal growth, these will typically be produced in a polycrystalline phase with quite small grain sizes (a few microns at best). In this case, the optical fiber can suffer from high scattering losses.

The second fabrication method is molten core fiber drawing (MCD), which has been adopted more globally because it offers high yields and lower production costs.[32-36] The fibers are drawn from a preform that consists of a glass cladding tube and a semiconductor material core that can be inserted into the pore in the form of a solid rod or powder. The preform is heated above the glass transition temperature of the cladding (>2000 °C for silica), which is high enough to melt the semiconductor core material. The softened glass cladding encapsulates the molten semiconductor material during the fiber drawing, preserving the cylindrical symmetry. As the fiber is drawn out of the furnace, it rapidly cools and the liquid core solidifies into a polycrystalline form. The core sizes of the MCD fibers are relatively large compared to those produced by HPCVD (tens of micrometers in diameter, or larger), but subsequent tapering

can be used to reduce the size of the cores down to the micrometer sizes required for infrared waveguiding.[37] The key advantage of the MCD method is that kilometer long fibers of elemental or compound group IV semiconductors can be drawn in a single process. A schematic showing semiconductor core fiber production via the MCD method is depicted in Figure 2c, and an optical microscope image of an as-drawn SiGe core fiber is shown in Figure 2d.[23] Due to the high temperatures the fiber is exposed to during the process, oxygen getters or interface modifiers are required to eliminate oxygen in-diffusion to the core from the cladding.[38] The MCD method also produces polycrystalline core materials, due to difficulty in controlling the cooling rate of the high temperature process. However, when compared to the HPCVD fibers, the crystal grain size is usually larger (can be millimeters in length), resulting in slightly improved material and optical properties, but still below acceptable levels for most photonic applications.[39]

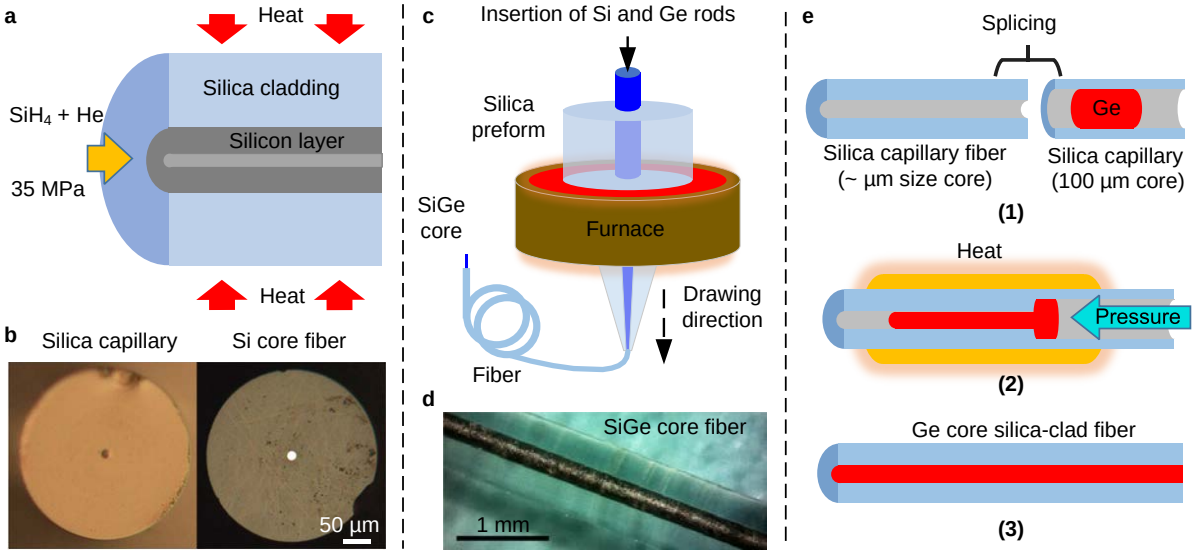

Figure 2. a) Schematic showing Si deposition within the void core of a silica capillary via a HPCVD process. **b)** Optical microscope images showing a silica capillary and the resultant Si core fiber after HPCVD. Reprinted with permission.[29] Copyright 2016, American Chemical Society. **c)** Schematic showing the MCD method. **d)** Optical microscope image of an as-drawn SiGe core silica-clad fiber. Reproduced under terms of the CC-BY license.[23] Copyright 2016, The Authors, published by Springer Nature. **e)** Schematic showing the PAMF method used for fabrication of a germanium core silica cladding fiber.

Another emerging method to produce semiconductor core fibers is the pressure-assisted melt-filling (PAMF) method,[40-42] which is similar to HPCVD. However, as the name implies,

the molten material is forced to infiltrate into the micron-sized pore of a silica capillary at high pressures, as schematically shown in Figure 2e for a Ge core fiber. Obviously, the melting temperature of the core material should be lower than the glass transition temperature of the silica capillary. Therefore, fabrication of Si core fibers by PAMF is challenging due to silicon's relatively high melting temperature. On the other hand, Ge, Sn, and their alloys, as well as other materials with low melting temperatures, including chalcogenide glasses and metals like gold, are compatible with PAMF. Typical outer diameters for the capillaries used in this approach are ~200 μm, and the pore size to be filled can be as small as 1 μm. As for the previous methods, the crystallinity of the core material cannot easily be controlled during the filling process, resulting in a polycrystalline material. Thus, the common theme for all of the semiconductor fiber production methods is that they require post-fabrication thermal processing to improve the material and optical quality of the fibers.

2.2 Laser annealing and crystallization of semiconductor core glass-clad fibers

Monocrystalline semiconductor core optical fibers are of great interest for the realization of all-fiber optoelectronics, because of their superior electrical, optical and thermal properties compared to those of amorphous and polycrystalline cores. Therefore, two primary approaches have been developed to date for post-fabrication laser annealing and crystallization of semiconductor core glass-clad fibers: i) direct melting of the semiconductor core via optical absorption of laser irradiance, and ii) indirect melting of the core via thermal conduction from the heated glass cladding. In the first case, a laser source emitting at UV or visible wavelengths, where the photon energy is larger than the electronic bandgap of the semiconductor but less than that of the cladding, is used, so that the light is strongly absorbed by the core. In general, crystallizing only the core with minimum softening of the glass cladding helps to reduce oxygen contamination, particularly when an interface modifier is absent. However, keeping the cladding rigid during laser processing induces residual tensile stresses within the core, due to the thermal expansion mismatch between the semiconductor core and glass cladding. In the

second case, a laser emitting light in the mid-infrared spectral region, where the glass cladding has high optical absorption, is used, so that the accumulated heat is transferred to the core via thermal conduction. Softening of the cladding during laser processing reduces the risk of cracking and the buildup of residual stresses on the core, though at the expense of increased laser power required for the crystallization and a greater chance of oxygen contamination.

As schematically shown in **Figure 3a**, for the short wavelength light, solidification occurs in the core at the trailing edge of the laser-induced molten zone, following the scanned beam focused on the fiber core. An example for CW argon-ion laser crystallization of an amorphous Si (a-Si) core fiber produced by HPCVD can be seen in the optical microscope image (Figure 3b),[43] where the structural change is evident from the color contrast in the transmission. The transmission electron microscope (TEM) micrograph of the single crystal Si (c-Si) core (Figure 3c) shows that the core/cladding interface is well defined within a 1 nm range. Similar to the bulk growth of semiconductors via directional crystallization, the quality of laser crystallization in semiconductor core fibers is determined by the maximum temperature, thermal gradient at the crystallization front, and cooling rate. These parameters are functions of the laser power and scan speed, which can be experimentally controlled. The laser power should be high enough to melt the entire semiconductor core, but low enough not to cause any vaporization and chemical reaction with the cladding, which would impair single crystal formation. By way of example, for the Si core fibers this temperature range is 1400-1600 °C. On the other hand, a large thermal gradient and a fast scan speed are required to stabilize the solid/liquid interface and arrest nucleation ahead of the crystallization front, respectively. However, increasing the scan speed while keeping the power constant decreases the thermal gradient, as inferred by finite element modeling.[43] Moreover, thermal supercooling and subsequent interface instability can occur if the scan speed exceeds a critical growth rate. Therefore, it is clear that there are optimum ranges for the laser power and scan speed (in this case 0.4-0.8 W and 1-3 mm s^{-1}, respectively), which allow for long lengths of c-Si core fibers,

corresponding to the gray area in the laser processing diagram (Figure 3d). The lowest optical loss measured at a wavelength of 1550 nm for a 1.7 µm diameter c-Si core fiber, which was laser-crystallized with a power of 0.45 W at a scan speed of 1 mm s^{-1}, is 0.47 dB cm^{-1}, a value which is approaching the best losses reported in conventional SOI waveguides. As expected for visible laser processing where the softening of the cladding is minimized, residual tensile stresses occur due to the thermal expansion mismatch between the Si core and glass cladding, which will be discussed in more detail in **Section 2.3**.

Visible laser crystallization has also been applied to a-Ge core fibers.[44] The a-Ge fiber had a core size of 5.6 µm and was processed using a laser power of 0.45 W, at a scan speed of 1 mm s^{-1}, to produce a high quality c-Ge core with grain sizes as long as 9 mm. Figures 3f,g show the cross-sections of the Ge fiber before and after crystallization. The TEM micrograph in Figure 3h shows the interface roughness after laser crystallization of the a-Ge core fiber. A remarkable reduction in optical losses (down to 1.33 dB cm^{-1}) at a wavelength of 2 µm has been achieved by laser crystallization of the a-Ge fiber, as compared to the un-processed a-Ge:H core fibers produced by HPCVD in Figure 3i.

CO_2 gas lasers have also been applied for laser crystallization of as-drawn Si, Ge, SiGe[23] and SnSe[24] core fibers, using the characteristic radiation at 10.6 µm where the glass cladding has high optical absorption. A schematic for a typical experimental setup used for laser processing of poly-Si core fibers is shown in Figure 3j.[45] The cross-section of a Si fiber with a 12 µm core that has been crystallized at a laser power of 14 W is shown in Figure 3k. An optimal range for both laser power and scan speed also exists for the case of laser crystallization via indirect core heating. It was found that the fibers laser-processed either at low scan speeds or low powers (100 µm s^{-1} and < 10 W, respectively, for this fiber type) had optical losses >20 dB cm^{-1}, similar to the losses in un-processed fibers. The optical losses measured at a wavelength of 1550 nm, as a function of the laser power and cooling rate at three different scan speeds, are shown in Figure 3l,m. A minimum optical loss of 2 dB cm^{-1} was achieved, though

the loss values seemed to level off at powers higher than 14 W and scan speeds faster than 3 mm s^{-1}. However, this trend is expected to reverse, i.e., optical losses increasing, if excessively large powers are applied introducing structural defects in the core, as demonstrated for a Ge core fiber crystallized by a CO_2 laser.[46] On the other hand, scan speeds higher than a critical speed could also adversely affect the crystallization of the unary semiconductor core, due to thermal supercooling inducing dendritic solidification.

In addition to the work on elemental group IV materials, some efforts to laser process alloyed SiGe core fibers have also been made. Processing of multi-constituent materials offers new possibilities in terms of compositional tuning of the core, however, there are some challenges originating from the different thermophysical properties of each element in the core. For example, constitutional undercooling, which occurs at high fiber drawing speeds, results in an instability of the solidification interface, so that SiGe core fibers produced by MCD have non-uniform composition distributions in the core with segregated Ge-rich and Si-rich regions. This is illustrated in the energy dispersive X-ray (EDX) analysis of the cross-section of an as-drawn SiGe core fiber shown in Figure 3n.[23] Laser crystallization at scan speeds relatively slower than those used in fiber drawing can be used to homogenize the core composition (Figure 3o). More details regarding the compositional segregation occurring in compound semiconductor fibers during laser processing will be given in **Section 2.4.**

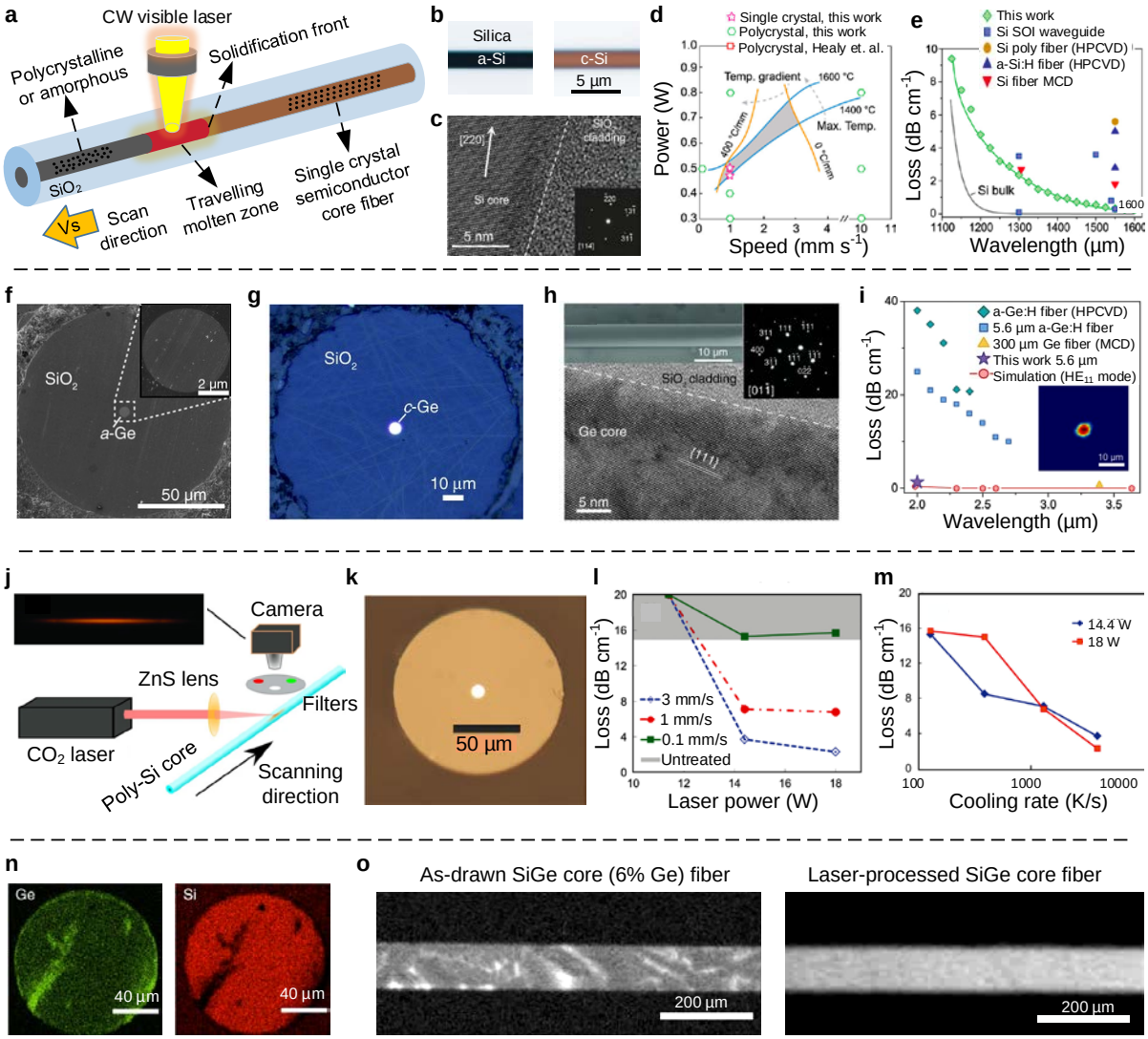

Figure 3. a) Schematic showing CW visible laser crystallization of a semiconductor core glass-clad fiber. **b)** Optical microscope image showing the color contrast between a-Si and c-Si in the core. **c)** TEM micrograph showing the c-Si core and amorphous cladding. **d)** Laser processing diagram showing optimum parameters (gray area) resulting in a single crystal core. **e)** Optical losses compared for various Si waveguides. **(b-e)** Reprinted with permission.[43] Copyright 2017, American Chemical Society. SEM micrograph and optical microscope image showing the cross-sections of **f)** an a-Ge core, and **g)** a laser-crystallized c-Ge core, respectively. **h)** TEM micrograph showing the lateral cross-section of a laser-crystallized c-Ge core fiber. **i)** Optical losses compared for various Ge core fibers. **(f-i)** Reproduced with permission.[44] Copyright 2016, Wiley-VCH Verlag GmbH & Co. KGaA, Weinheim. **j)** Schematic showing CO_2 laser annealing of a poly-Si core fiber. **k)** Optical microscope image showing the cross-section of the crystallized Si core fiber. Optical losses obtained at different **l)** laser powers for various scan speeds and **m)** cooling rates for various powers. **(j-m)** Reproduced with permission.[45] Copyright 2016, The Authors, published by Wiley-VCH Verlag GmbH & Co. KGaA, Weinheim. **n)** EDX micrographs showing non-uniform distribution of Ge and Si in the cross-section of an as-drawn SiGe core fiber. **o)** XCT images showing the distribution of the composition in the longitudinal cross-section of a SiGe core fiber before and after laser annealing. **(n,o)** Reproduced under terms of the CC-BY license.[23] Copyright 2016, The Authors, published by Springer Nature.

2.3 Laser-induced strain and bandgap engineering in unary semiconductor core fibers

The transmission window of Si spans a wavelength range of 1100-8000 nm. Whilst this makes it useful for light transmission across the telecom bands, it offers limited functionality in terms of optical detection. However, it was demonstrated by Healy et al.[47] that extreme tensile stresses can be induced in a c-Si core fiber by using localized laser heating of an a-Si core, which significantly alters the optoelectronic properties of the fiber. These residual stresses emerge because c-Si is denser than a-Si, causing the material to shrink, but at the same time the core stays firmly attached to the rigid native oxide cladding. Moreover, it was shown that the residual stresses were a function of the scan speed (which essentially translates to how much heat is transferred to the cladding), thus enabling engineering of strain, and hence electronic bandgap, along the Si core fiber. **Figure 4a** shows Raman spectra of two 1.7 µm diameter c-Si core silica-clad fibers, which were crystalized by laser processing at scans speeds of 0.1 mm s^{-1} (F2) and 1 mm s^{-1} (F1), showing how this maps to the induced strain. Photoconductivity measurements, which were carried out as schematically depicted in Figure 4b, indicate a bandgap reduction from 1.05 eV to 0.59 eV (Figure 4c), enabling optical detection up to a wavelength of 2.1 µm. On the other hand, as laser-induced strain is a deformation of the cubic crystal, resulting in isotropic and anisotropic components within the core, the centrosymmetric crystal structure of the Si is also modified. This opens a route to writing a sizable $\chi^{(2)}$ in c-Si core glass-clad fibers for second order nonlinear optical processes[48] and linear electro-optic modulation (Pockels effect).[49] Therefore, by using laser-induced spatial modulation of the strain and bandgap in the core, highly efficient detectors, low-loss optical waveguides, and high speed modulators could be integrated in c-Si core glass-clad fibers.

Local strain modification by laser processing can also be used for engineering the refractive index in the semiconductor core fibers. Recently, a Bragg grating was written into a post-processed c-Si core, silica clad fiber using a 220 fs laser emitting at 517 nm and 5 kHz to induce a periodic strain profile at the core/cladding interface.[50] The focused laser spot of l µm

diameter was raster scanned across the core at a speed of 50 µm s^{-1}, while the fiber was moved step by step by translating the stage in the axial direction, as illustrated in Figure 4d. Discrete movements of the stage correspond to the period (1820 nm) of an 8th order Bragg grating, which has a reflection spectrum with a linewidth of 0.9 nm at a wavelength of 1565 nm (Figure 4e). During the laser writing, a strong plasma was also observed as shown in the inset figure. Importantly, the use of a 517 nm wavelength femtosecond laser enables strain and refractive index modification at the core/cladding interface without significantly compromising the quality of the c-Si core, because of the small optical penetration depth and ultrashort duration of the heating process. However, inscription of first-order Bragg gratings remains a challenge by this line-by-line laser writing process, due to the diffraction-limited laser spot size.

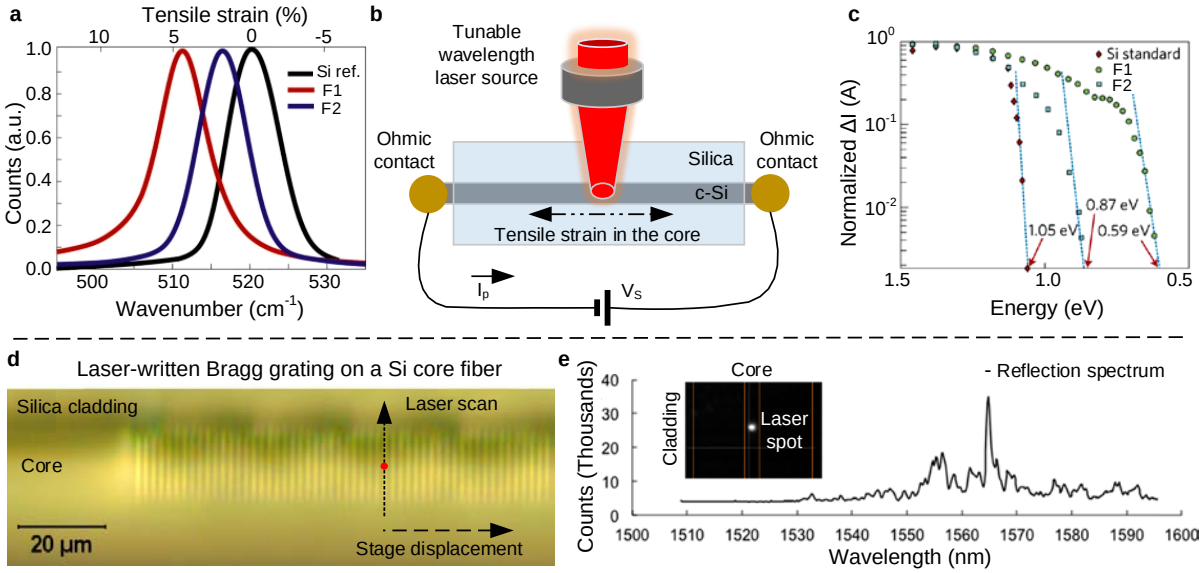

Figure 4. a) Raman spectra showing the effect of residual tensile strains for two laser-processed c-Si core fibers using different scan speeds of 1 mm s^{-1} (F1) and 0.1 mm s^{-1} (F2). **b)** Schematic showing the experimental setup used for current and voltage (I-V) measurements at different excitation wavelengths. **c)** Bandgap shifts of the c-Si core fibers shown in **(a)**. **(a,c)** Reproduced with permission.[47] Copyright 2014, Springer Nature. **d)** Laser-written 8th order Bragg grating reflector with a period of 1820 nm, and **e)** its reflection spectrum. Inset figure shows the plasma created by the laser spot during laser writing. **(d,e)** Adapted with permission.[50] Copyright 2017, The Optical Society.

2.4 Laser-induced phase segregation for composition engineering in compound semiconductor core fibers

There is growing interest in fibers with compound semiconductor cores consisting of binary alloys to extend the operational wavelength range and increase the diversity of applications.[23,24] Moreover, it is also possible to tune the bandgap and optical properties, which depend on the precise composition of the constituents,[51] both before and after the fiber fabrication. Initially, the stoichiometry of a semiconductor alloy core is determined by either setting the flow ratio of precursors during the HPCVD process or adjusting the mole fraction of the semiconductor elements inserted into the core at the preform preparation stage. Subsequent laser thermal processing allows for post-process on-demand tunability of the local composition along the core, as well as improvement of the crystallinity and homogenization, as discussed earlier. Owing to the small, micron scale, laser-induced heat zone within the core, large thermal gradients ($1\text{-}2\times10^4$ K cm^{-1}), as well as fine control over the scan speed (1-1000 μm s^{-1}) and optical power, it is possible to achieve precise, nano/micron scale, adjustments of the composition in the core.

Of the various compound semiconductor fibers that have been produced to date, SiGe is the most straightforward core material to fabricate, making it the prime candidate for application of laser post-processing to engineer the composition, bandgap and refractive index. However, SiGe alloys present challenges for laser processing because of the large gap between the liquidus and solidus in the equilibrium phase diagram.[52] When a molten zone is induced in an initially homogenous SiGe alloy by laser heating, compositional separation of Si and Ge elements spontaneously occurs at the interface of the coexisting liquid and solid phases, which is referred to as phase segregation. As the solubility of Ge is higher in the liquid phase, the excess Ge at the liquid/solid interface quickly diffuses away into the molten zone, making it Ge-rich, and the solidified region surrounding the molten zone becomes Si-rich as a result of phase segregation.

If the molten zone shrinks in size, for example by slowly decreasing the laser power absorbed in the core, it gathers more Ge and eventually solidifies with a higher Ge content when the temperature drops below the melting temperature. By using laser-induced phase segregation, a 35 at.% Ge region was obtained on the side of a 6 at.% Ge core fiber, by slowly defocusing a CO_2 laser beam,[23] as shown in the X-ray computed tomography (XCT) images in **Figure 5a,b**. On the other hand, if the laser beam is scanned along the core, it produces a travelling molten zone with an increasing Ge composition, which eventually saturates at a dynamic equilibrium where the solidified core at the trailing edge has the same initial Ge composition as in the un-treated SiGe core. This provides a mechanism to obtain a homogenous core all the way down to the other distal end of the fiber, using laser scanning at low constant scan speeds (<10 μm s^{-1}). Periodic Ge-rich regions (Figure 5c) can also be created in the core by using transient effects such as on-off modulation of the laser power (Figure 5d), which basically corresponds to the acceleration of the solidification front. Similarly, by focusing a laser beam vertically on the top end of a SiGe fiber (Figure 5e) and applying a stepwise reduction of the power, Ge-rich caps on the SiGe core fiber can be obtained, as shown in the Figure 5f.[53]

For stable growth from the solidification front following the laser-induced molten zone in a SiGe core fiber, the laser scan speed has to be smaller than a critical value, which depends on the local temperature gradient, composition, and thermophysical properties of the alloy in the core. Otherwise, constitutional undercooling can emerge ahead of the solid/liquid interface, breaking its stability.[23] Consequently, the interface instability results in dendritic structures during laser annealing of the SiGe core fibers, leading to a random spatial redistribution of the composition. This is shown in Figure 5g where cross-sectional images of SiGe core fibers are displayed for laser crystallization at increasing scan speeds.[54] Here the brighter regions represent Ge-rich regions. In contrast, under stable growth conditions, if convective cooling of a SiGe core fiber is established by a forced air flow around the fiber, radially symmetric compositional structures in the core can be obtained by laser thermal processing (Figure 5h). A

graded-index (GRIN) SiGe core with a Ge-rich center is shown in Figure 5i. However, it is important to note that laser-assisted compositional engineering is not limited to the group IV semiconductor core fibers. For example, incorporation of III-V semiconductors, such as GaSb, into Si core materials offers new avenues for the formation of direct bandgap regions in the core by laser-induced phase segregation, as shown in Figure 5j.[55] EDX elemental maps (Figure 5k) show the composition of the phase-segregated regions in the core along the fiber corresponding to A and B positions, where the dominant semiconductor materials in these regions are Si and GaSb, respectively. The ability to produce isolated III-V compound semiconductors within the Si core is an important step towards incorporating light sources and detectors within Si core optical fibers.

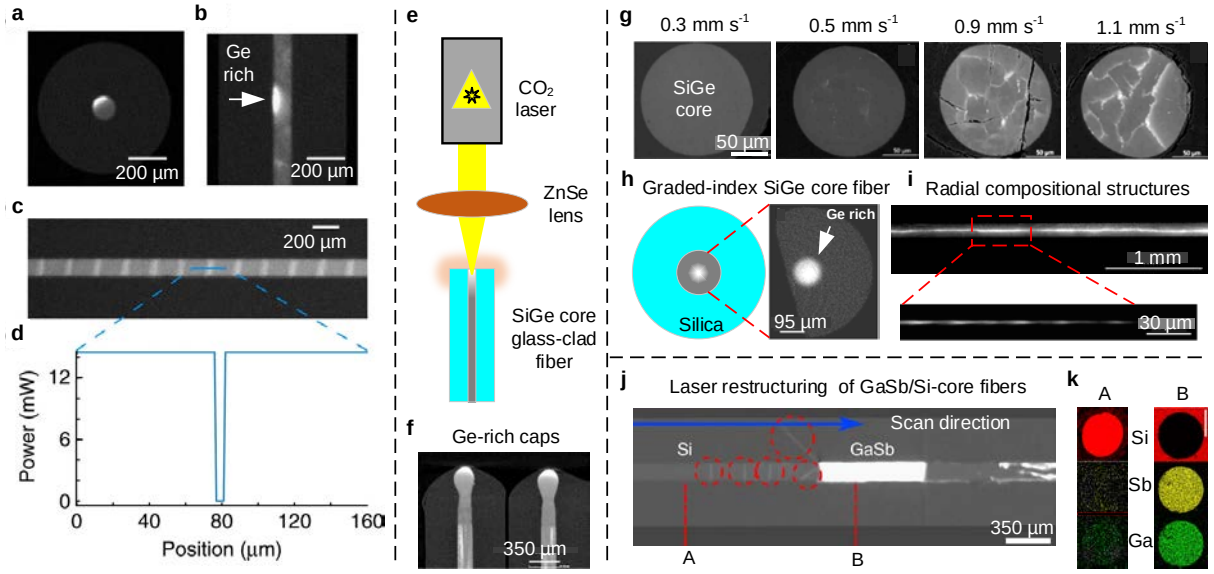

Figure 5. XCT images showing phase segregation in the **a)** transverse and **b)** longitudinal cross-sections of laser-processed SiGe core fibers. **c)** Periodic Ge-rich regions written within the core by **d)** modulation of the laser power. **(a-d)** Reproduced under terms of the CC-BY license.[23] Copyright 2016, The Authors, published by Springer Nature. **e)** Schematic showing laser processing of the end facet of a SiGe core fiber. **f)** XCT image showing Ge-rich caps formed on the tips of SiGe fibers. Adapted with permission.[53] Copyright 2019, The Optical Society. **g)** XCT images of the fiber cross-sections showing the effect of laser annealing on the compositional homogeneity of a SiGe core fiber at different scan speeds. **h)** Schematic and XCT image showing the cross-section of a laser-processed SiGe fiber, which was exposed to radially symmetric convective cooling. **i)** XCT image of the longitudinal cross-section showing radially symmetric concentration gradients obtained along the SiGe core. **(g-i)** Adapted with permission.[54] Copyright 2020, The Optical Society. **j)** Laser-induced phase segregation in a GaSb/Si core fiber. **k)** EDX showing elemental compositions at A and B positions marked on the fiber. Scale bar is 100 µm. **(j,k)** Reproduced under terms of the CC-BY license.[55] Copyright 2019, The Authors, published by Springer Nature.

2.5 Laser-induced thermocapillary instability in semiconductor core glass-clad fibers

The formation of microspheres that arise from the break-up of a fiber core due to Plateau–Rayleigh (PR) instability during thermal processing is a useful method to produce micro/nano particles for optoelectronic and photonic applications. First observed in chalcogenide glass core fibers,[56] several examples have now been demonstrated using semiconductor core fibers.[57] In contrast to the previous examples of laser crystallization of the semiconductor fiber cores, here higher power CO_2 lasers are employed to liquefy the glass cladding so that surface tension dominates the viscous forces, initiating thermocapillary instability in the core, as schematically illustrated in **Figure 6a.**[58] Figure 6b shows an ordered array of Si microspheres within a glass cladding after laser thermal processing.

With regard to microstructuring, laser thermal processing provides unique advantages compared to isothermal furnace heating[59] and axial thermal gradient heating via a flame.[60] For example, the length of the heat zone, maximum temperature, and thermal gradient can be precisely controlled, which helps to avoid small satellite sphere formation between the primary spheres.[59] By modifying the laser power and scanning velocity (or fiber feed-in velocity), it has been demonstrated that both the size of the particles and the induced residual stresses can be engineered.[61] An immediate application of the resulting Si microspheres is to exploit them as whispering gallery mode (WGM) resonators, as shown in Figure 6c, where the Si microsphere was released from the glass cladding by hydrofluoric (HF) acid etching. Transmission spectra for a wavelength range of 1561-1564 nm and a resonance dip at a wavelength of 1563.34 nm are given in Figure 6d,e.[61] The quality factor of the WGM Si microresonator was measured to be 7.1×10^5, demonstrating that high-quality (high crystallinity and low loss) microcavity resonators can fabricated by using laser-induced PR instability in semiconductor core glass-clad fibers. It is also possible to transfer these arrays of microspheres to planar substrates without compromising their positional order and spherical symmetry by

applying a similar technique used for on-chip integration of chalcogenide glass microspheres produced in a polymer-clad fiber.[59]

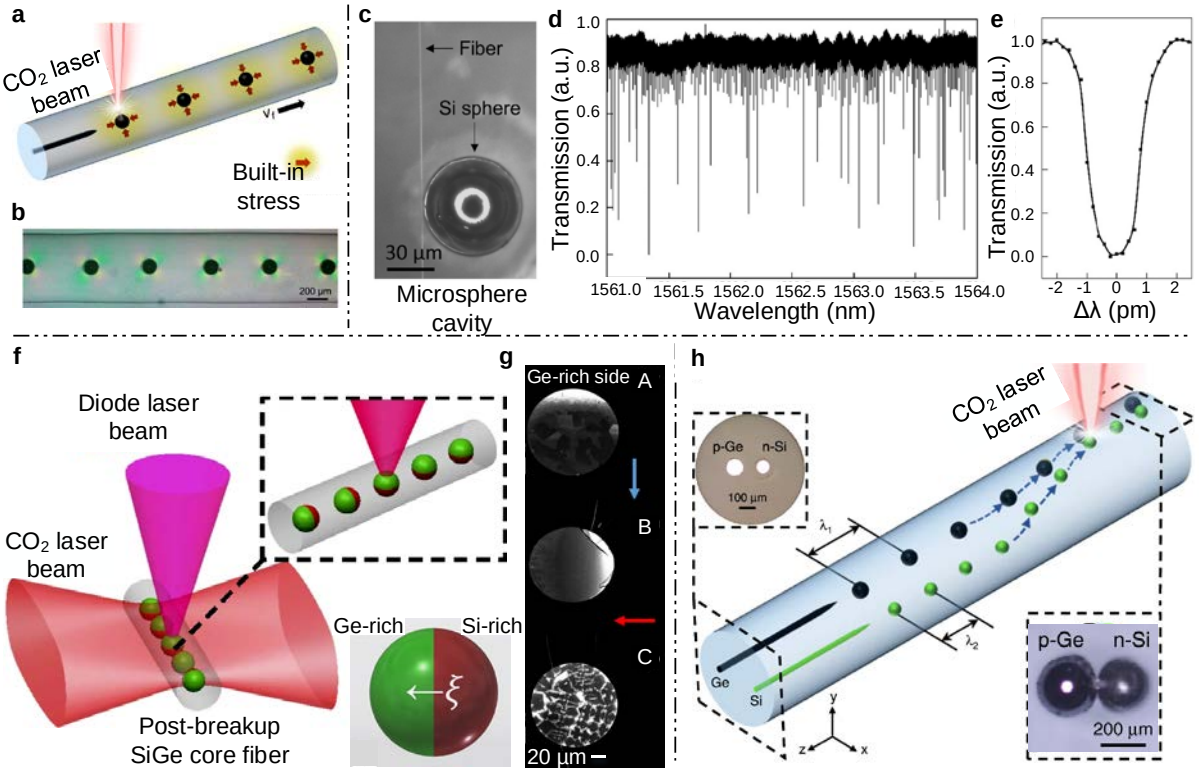

Figure 6. a) Schematic showing laser-induced PR instability in a semiconductor core glass-clad fiber. **b)** Optical microscope image showing an array of Si micro-spheres encapsulated by a glass cladding after the core breakup. **(a,b)** Reprinted with permission.[58] Copyright 2019, American Chemical Society. **c)** A tapered silica fiber is used for optical coupling into a Si microsphere resonator. **d)** Transmission spectrum of the Si microsphere resonator and **e)** a zoomed-in spectrum at a resonance wavelength of 1563.34 nm. **(c-e)** Reproduced with permission.[61] Copyright 2017, Wiley-VCH Verlag GmbH & Co. KGaA, Weinheim. **f)** Dual laser treatment of SiGe microspheres in a glass-clad fiber. **g)** SEM micrographs showing the cross-sections of Janus microspheres with Ge-rich (bright) and Si-rich (dark) regions, which were cooled at (A, B) slow and (C) fast shut-off rates of the laser power. Arrows show the direction of the diode laser beam (purple), which was used to control the cooling rate. **(f,g)** Reproduced with permission.[62] Copyright 2017, National Academy of Sciences. **h)** Schematic showing positional manipulation of the Ge and Si microspheres within a glass-clad fiber via laser-driven thermocapillary convection. Reproduced under terms of the CC-BY license.[63] Copyright 2019, The Authors, published by Springer Nature.

In addition to mass production of spherical particles, laser thermal processing can also be used as a post-breakup treatment for the fiber, for example, to control phase segregation in semiconductor alloy particles via the cooling rate, or to manipulate the position of single or multiple microspheres in the cladding. Using a dual laser arrangement schematically illustrated in Figure 6f, softening of the glass-clad fiber and the solidification rate of the SiGe microspheres

can be independently controlled by a CO_2 laser and a visible diode laser, respectively. SiGe Janus particles with non-dendritic Ge-rich and Si-rich regions can be produced using slow shut-off rates for the diode laser, as shown in Figure 6g,[62] where the arrows in A and B correspond to the direction of the diode laser beam. On the other hand, abrupt shut-off rates result in cellular or dendritic microstructures shown in the subfigure C in Figure 6g, due to the interface instability and constitutional undercooling occurring after the fast cooling. By using laser-induced thermocapillary convention, single or multiple microspheres can be migrated toward any desired position in the cladding, enabling formation of heterojunctions between n-doped Si and p-doped Ge microspheres (Figure 6h).[63] This is an important capability for fabrication of optoelectronic devices within semiconductor core glass-clad fibers.

2.6 Future prospects for laser-processed semiconductor core fibers

There are numerous potential directions for further development in laser thermal processing of semiconductor core glass-clad fibers along the lines discussed above. Here we highlight some new directions of travel where there could be significant impact.

2.6.1 *Laser thermal processing of compound semiconductor core fibers for index modulation*

As of to date, laser induced composition engineering in compound semiconductor core fibers has been limited to SiGe alloy core fibers processed via CO_2 lasers. However, visible lasers can provide direct heating of the alloy core through the glass cladding, enabling more flexibility to control the solidification rate and the size of the heat zone. Moreover, if the core is directly heated instead of the cladding, more efficient cooling of the fiber cladding via forced air convection can be achieved, which is required to obtain a radially symmetric Ge-rich region in the center of the core. On the other hand, laser writing of axial and radial compositional structures could be achieved using fibers with cores made from other pseudo-binary alloys, such as ternary semiconductor alloys ($Al_xGa_{1-x}As$), which have isomorphous equilibrium phase diagrams similar to that of the SiGe alloys. Additionally, to further increase the Ge content in the core region solidified after the acceleration of the solidification front, faster transient effects

can be accomplished during laser scanning by using electro-optic beam modulators/deflectors or acousto-optic beam scanners, which can operate at MHz rates.

2.6.2 *Laser processing of Sn-based compound semiconductor core fibers for lasing applications*

Semiconductor alloys with tin, such as SiGeSn and GeSn, have recently been attracting great interest within the planar photonics community because alloying with Sn (>8 at.%) allows for a real direct bandgap compound needed for the construction of light sources and photodetectors.[64-66] However, the fiber community is yet to take full advantage of Sn-based alloys, with only one example of incorporating Sn as a interfacial metallic layer around a Ge core fiber to date.[67] Laser processing could be used to complement the fabrication of these fibers, both by improving the crystalline quality of the core, but also by writing in tensile strains to tune the bandgap post-fabrication. For example, laser crystallization has been demonstrated to achieve residual tensile strains up to 4% in a c-Si core fiber[47], and relatively lower uniaxial tensile strains (2%) could be sufficient to achieve a pseudo-direct bandgap in Ge core glass-clad fibers. Similarly, residual tensile strains would facilitate the indirect-to-direct bandgap conversion in laser-processed GeSn core fibers with Sn contents lower than the equilibrium solubility of Sn (<1 at.%). This could prove to be a useful way to develop semiconductor core fiber lasers and amplifiers for the wavelength range of 2.0-2.4 μm,[68] which is becoming increasingly important for broadband communications. However, there are significant challenges for laser annealing of as-drawn Sn-doped semiconductor fibers, due to the extreme segregation of Sn and constitutional supercooling, which can be prohibitive.

2.6.3 *Laser-induced in-fiber reactive phase transformation from Al to Si core fibers*

Reactive fiber drawing is an emerging fabrication method, which allows for the production of fibers that have completely different constituents to the preform composition and structure.[69] For example, starting with a metallic aluminum (Al) core, a silica-clad preform was drawn into a Si core fiber.[70] At high temperatures, the Al core reacts with the SiO_2 cladding to produce Si in the core and a surrounding Al_2O_3 interfacial layer. As an alternative fabrication method,

micrometer-sized Al core fibers could be produced directly by pressure-assisted melt filling of Al into the pore of a silica capillary, as Al has a melting temperature lower than that of silica. Subsequently, local laser heating could be used to induce a reactive phase transformation of Al to produce a Si core, with axial modulation of the core from metal to semiconductor along the fiber. The ability to produce Si from cheap Al and silica by local laser processing could be a simple method to incorporate both metal and Si inside the fiber geometry for integrated photonic and optoelectronic devices.

2.6.4 *Laser fusion of Si core fibers and planar waveguides for fiber-to-chip optical coupling*

Semiconductor core fibers (SCFs) can be directly spliced to conventional single mode fibers (SMFs) [71,72]. However, these methods suffer from high losses due to the mode mismatch and fragility of the splice. To address these issues, integration of tapered Si core glass-clad fibers to tapered SMFs has been demonstrated by using Si nano-spike couplers at the splice joint.[73] Although an optical coupling loss of 4 dB was achieved in this first attempt, it was shown by using simulations that the coupling losses could be reduced below 1 dB by optimizing the core-to-cladding ratio and tapering parameters. Unlike the SCF-to-SMF connection, integration of SCFs to their planar waveguide counterparts has yet to be demonstrated. However, as conventional splicing cannot be used for planar platforms, laser fusion of an end-tapered Si core fiber with the facet of an on-chip Si waveguide could be an option to realize permanent and effective optical coupling, which is in high demand for low-cost integration of packaged photonic devices to conventional fibers.

3. Laser-processed planar photonic devices

Owing to their low cost, energy efficiency, and small footprints, integrated planar photonic systems offer several advantages over their fiber-based counterparts across application areas that require high densities of components. These systems typically consist of various active and passive optical components, which can be produced from both elemental and compound semiconductors, either epitaxially grown as a monocrystalline material on crystalline substrates,

or deposited in amorphous and polycrystalline phases on glass substrates, depending on the deposition temperature. Of all the different integrated material platforms, over the past two decades silicon photonic systems have become the most widely developed thanks to their compatibility with Si-based microelectronic processors. However, owing to the limited photonic functionality of Si, there is currently an increasing impetus towards incorporating other group IV semiconductors, such as Ge and Sn, within these systems to modify, enhance and/or expand the optical and electrical characteristics.[74-76] Similar to the fiber materials, many of the fabrication methods applied to produce multi-material, multi-functional integrated planar systems require post-processing thermal treatments to improve the quality and thus performance of the system. Whilst furnace treatments, such as rapid thermal processing (RTP), are the most widely used approach, these cannot be applied locally to individual components, and they also lack the precision needed to fine tune the operating characteristics of devices. Thus, in recent years there has been growing interest in adapting laser processing treatments for the specific purpose of developing flexible fabrication approaches for planar photonic systems. We start this section with a brief introduction to commonly used deposition and growth methods for group IV semiconductors before highlighting some of the most important applications of laser thermal processing on planar photonic systems.

3.1 Primary deposition and growth methods for group IV semiconductor thin films.

Over the last decade, there has been growing interest to incorporate group IV elemental semiconductors (Si, Ge, Sn), as well as their binary (SiGe, GeSn) and ternary compounds (SiGeSn), within integrated photonic systems.[77-79] In particular, heterostructures, quantum wells, and superlattices made from group IV semiconductors are in high demand for photonic devices such as detectors, modulators, and lasers.[80-83] Methods for semiconductor growth can be grouped into two broad categories: physical vapor deposition (PVD) and chemical vapor deposition (CVD).[84] The most advanced and mature method of PVD is molecular beam epitaxy (MBE), which is a sophisticated form of vacuum evaporation.[85,86] A schematic

diagram of a MBE growth chamber is shown in **Figure 7a**. In MBE, neutral atomic and molecular sources, provided by effusion cells (Knudsen cells), are deposited on the surface of heated substrates under ultrahigh vacuum conditions. Using MBE, complex structures such as quantum wells and superlattices can be epitaxially grown by atomic layers, with precise control of their thickness, alloy composition, doping level, and in situ analysis via reflection high-energy electron diffraction (RHEED). The great advantage of MBE is that the stoichiometry of a compound semiconductor film is mainly determined by the flux ratios of the sources. The substrate temperature controls the surface morphology of strained or relaxed layers.

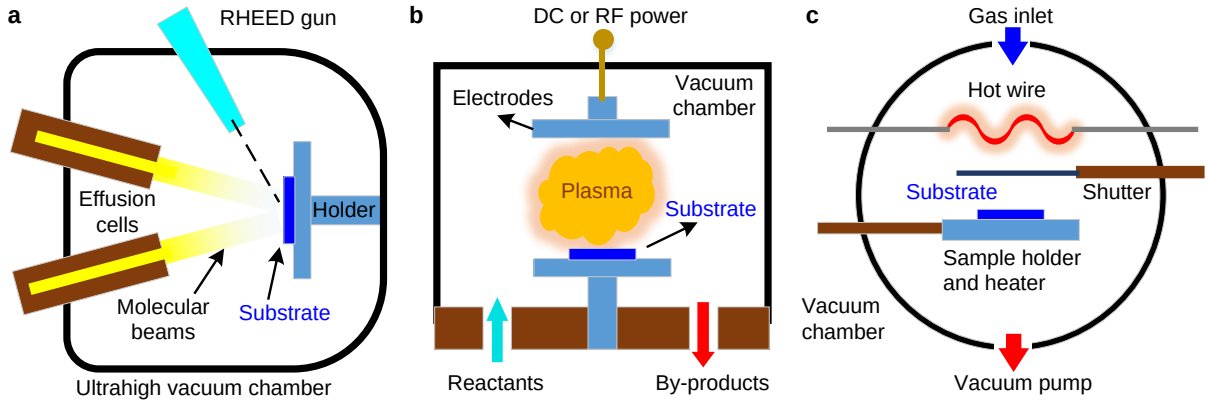

Figure 7. Schematics showing various components in the material growth chambers of **a)** molecular beam epitaxy (MBE), **b)** plasma enhanced chemical vapor deposition (PECVD), and **c)** hot-wire chemical vapor deposition (HWCVD).

On the other hand, material growth in CVD occurs when precursors, typically volatile gases such as SiH_4 and GeH_4, react via a chemical process near or on the surface of a substrate, resulting in deposition of the reaction product and removal of the gaseous byproduct.[87] CVD is a resourceful, but complex process, where the pressure, temperature, and flow rates of the precursors can all affect the growth rate and composition of the deposited films. Compared to MBE, CVD is less precise, but still the film thickness can be controlled down to sub-nanometers. However, CVD is capable of large area thin film deposition at lower costs, which is preferable for fabrication of high volume integrated photonic systems. Furthermore, the chemical reactions can be activated by thermal, laser-assisted, and plasma-assisted sources.[88] A schematic diagram of a plasma-enhanced CVD (PECVD) is shown in Figure 7b. The precursors are

decomposed in a plasma via the collisions between energetic electrons and gas molecules. The advantage of PECVD over thermal CVD is that the deposition of semiconductor films can be achieved at relatively low temperatures, [89,90] which is critical for complementary metal-oxide-semiconductor (CMOS) compatibility. Moreover, low temperatures enable growth at non-equilibrium conditions, which has been used to produce compound semiconductor films without phase segregation.

A relatively new version of the CVD process, which has recently gained popularity to deposit various materials on planar substrates for the fabrication of photonic components,[91,92] is hot wire CVD (HWCVD). A schematic configuration for the HWCVD process is shown in Figure 7c, where the precursors decompose on the hot filament to produce the deposition species.[93] Significantly, HWCVD not only allows for improved control over the deposition parameters such as deposition rate, but as the heating is largely confined to the wire, it allows for depositions at low substrate temperatures. Further advantages of HWCVD are:[94] i) the semiconductor films can be produced with higher deposition rates; ii) it enables more conformal deposition without any plasma-induced damage; and iii) it allows for deposition of highly condensed films with low hydrogen content. This latter point is particularly important for laser processing treatments to prevent violent out-diffusion of the hydrogen, which can cause significant damage to the films.

For epitaxial growth, MBE and CVD require crystalline substrates with lattice matching to that of the material to be grown. However, there are large lattice mismatches of 14.7% (19.8%) between Sn and Ge (Si), and 4.2% between Ge and Si. Therefore, a direct epitaxial growth of Ge, Sn, and their alloys on Si substrates results in either partially or fully relaxed thin films, with misfit and threading dislocations for film thicknesses above a critical value (<10 nm for Ge on a Si substrate) where the pseudomorphic structure becomes unstable. These crystal defects are detrimental to the performances of photonic devices, degrading electrical and optical properties. Similarly, dangling bonds and a large number of grains can lead to optical absorption

and scattering in amorphous and polycrystalline semiconductor films deposited on glass substrates. As a complementary process, laser thermal annealing and crystallization provides a post-deposition approach to enhance the structural, electrical, and optical qualities, as covered in the following section.

3.2 Laser annealing, crystallization, and reflowing of semiconductors on planar substrates for fabrication of optical waveguides

Poly-Si potentially offers similar electrical and optical properties compared to c-Si, but can be more flexibly produced on various substrates using the CVD-based deposition methods discussed above. This makes poly-Si a promising material for the fabrication of three-dimensional (3D) multilayered and multi-material photonic systems.[95,96] However, poly-Si optical components typically suffer from high absorption losses due to dangling bonds at the grain boundaries, as well as high scattering losses due to density fluctuations within the material and surface roughness. Therefore, either high temperature deposition (>1000 °C) of poly-Si films or post-deposition thermal annealing of a-Si films is required to reduce the number of grain boundaries, which serves to enhance the material, electrical, and optical properties of deposited films.[97,98] As an alternative to furnace annealing, where the entire chip is exposed to high temperatures, laser annealing provides localized heating, reducing the risk of damage to other components. For completeness, we note that CW and pulsed lasers have extensively been used to anneal semiconductors since the 1980's.[99] In particular, excimer laser annealing (ELA) has been used to crystallize large areas of a-Si films deposited on glass substrates leading to the fabrication of low-cost active-matrix-driven flat panel displays.[100]

A wide range of laser sources operating at UV, visible (VIS), and near infrared (NIR) wavelengths, in pulsed and CW modes, have been exploited to crystallize group IV semiconductors, including Si,[101] Ge,[102] SiGe,[103] and GeSn[104,105] thin films and components. These materials have been deposited both on crystalline (i.e., bulk Si) as well as on insulator substrates, which can be further exploited to alter the crystallization process. Irrespective of the

laser source, two different annealing regimes occur that are related to the laser power, which is adjusted to set the process temperature either below or above the melting point of the semiconductor thin film. Solid phase crystallization, i.e., low laser power, results in poor quality polycrystalline material with nanoscale-sized grains, and requires long hours of annealing (> 24 h at 600 °C). In contrast, high power processing that promotes liquid phase crystallization is employed to achieve better crystallinity within practical processing times (<1 h). This can be illustrated for the case of pulsed ELA, where the optimum crystallization condition occurs when the power is set to realize near complete melting of the film, such that nucleation seeds from small grains at the film/substrate interface, growing radially outwards.[106] Typical pulse durations for ELA are a few tens of nanoseconds. Short pulse durations are particularly advantageous to eliminate dopant diffusion, and intermixing effects at the interface.[107] In particular, if rapid solidification occurs far from equilibrium conditions, for example via nanosecond pulsed laser annealing of alloy thin films on substrates with high thermal conductivities such as silicon, this could allow for crystallization of supersaturated alloy thin films, for example, GeSn with a Sn content exceeding the equilibrium solid-solubility (> 1 at.%) in Ge.[108,109] However, it is worth noting that laser annealing of semiconductor alloys with higher Sn contents can suffer from effects such as surface segregation and cellular breakdown limiting the photonic applications.

On the other hand, the annealing time in CW laser crystallization (CLC) is on the order of milliseconds, as determined by the ratio of the spot size and scan speed. In this instance, the optimum condition to get large grains is achieved when the laser power is the close to the ablation threshold of the material.[110] The biggest advantage of CLC is that elongated grains in the direction of the laser scan are produced due to continuous lateral crystallization following the laser-induced molten zone, and the size of the elongated grains (~200 μm) is typically larger than those obtained in ELA (< 1 μm), due to the low cooling rates. In addition, it has been

demonstrated that the density of defects and number of dangling bonds in grain boundaries in CLC are smaller compared to those produced via ELA.[106]

Bulk Si platforms, which are widely employed by electronics industries, enables low-cost photonic integration compared to SOI substrates. Laser-crystallized poly-Si waveguides can be fabricated on bulk Si in several steps, as schematically shown in **Figure 8a**.[111] Oxidation of the trenches etched in bulk Si provides optical isolation similar to SOI substrates. After deposition of the a-Si thin film on the local buffer oxide (BOX) layer, lateral crystal growth can be seeded from the c-Si at the sides using thermal annealing, where both furnace and laser treatments have been explored. As the crystal growth laterally proceeds from both edges toward the center of the trench, there is a high number of grain boundaries in the center of the processed films where the growth fronts intersect. Therefore, the waveguide structures are subsequently patterned with an offset from the center to minimize the number of grain boundaries, and thus scattering losses, in the core. On the other hand, surface roughness-related scattering will still be present due to the patterning of the poly-Si waveguides after the crystallization process. So far, only the optical properties of the furnace annealed samples have been measured, revealing losses of 6.1 dB cm^{-1}. However, the losses are expected to be lower for the laser-processed waveguides, which were annealed by using a frequency-doubled (532 nm) high-power pulsed Nd:YAG laser, because the processed material quality was found to be as good as that of the bulk Si substrate when evaluating via TEM measurements.

Another way of integrating optical waveguides on bulk Si is lithographical patterning of the surface to produce c-Si fins, followed by laser processing (248 nm KrF excimer laser with a pulse duration of 25 ns and pulse energies up to 700 mJ) to reshape the top half and subsequent oxidation to produce a cladding,[112,113] as schematically illustrated in Figure 8b. Moreover, the laser thermal processing helps to reduce surface scattering losses after the patterning process by melting and subsequent reflowing of the c-Si waveguides due to the surface tension. However, so far these structures have only been produced using a large-area (4

mm×4mm), uniform (5% variation), static laser exposure, which can induce thermocapillary instability on the waveguides, creating long range surface undulations, similar to those observed within the cores of thermally annealed fibers, as discussed previously. Thus, the optical losses in these waveguides have been limited to values of 6.9 dB cm^{-1}.

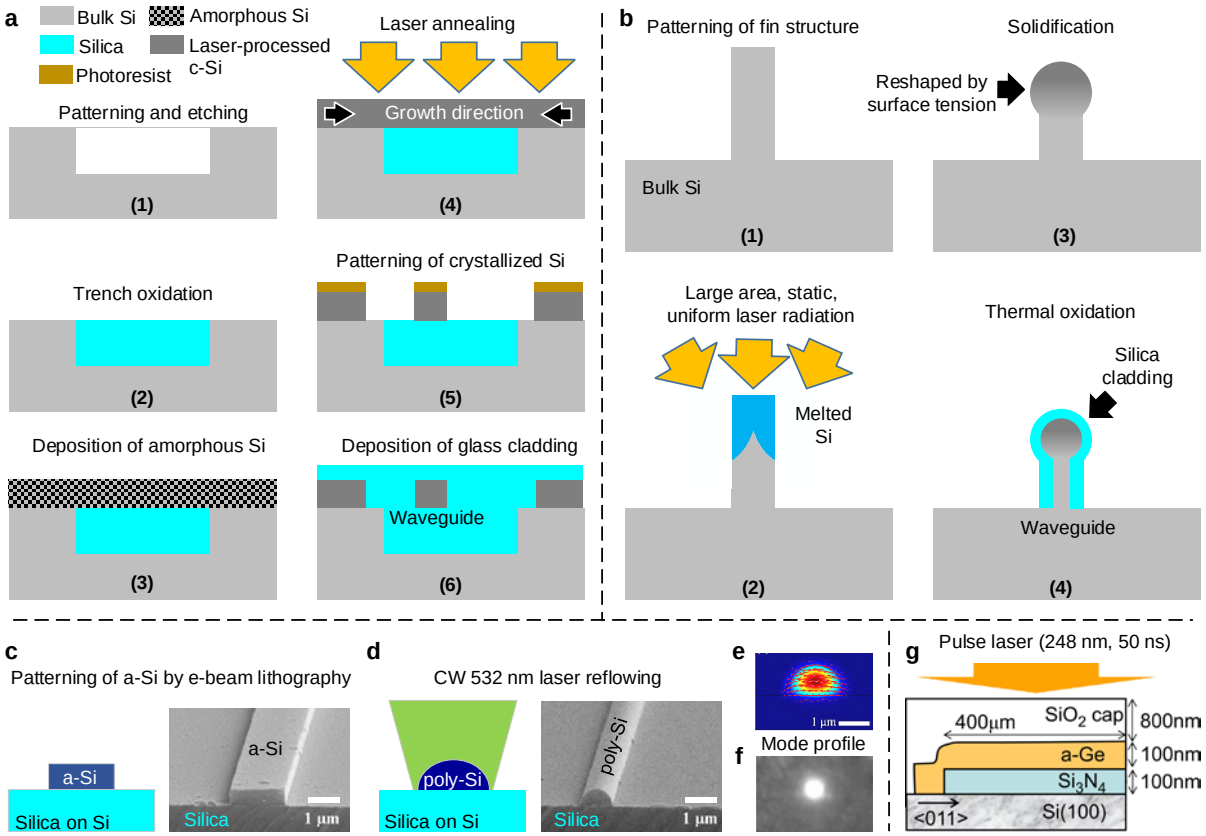

Figure 8. a) Fabrication steps to integrate laser-crystallized poly-Si waveguides on bulk Si substrates. **b)** Laser reflowing of patterned c-Si fin waveguides and their subsequent thermal oxidation to produce silica cladding layers. Schematics and SEM micrographs showing pre-patterned a-Si waveguides **c)** before and **d)** after laser annealing and reflowing. **e)** Simulated and **f)** experimental TE mode profiles of a poly-Si waveguide with a surface-tension-induced parabolic cross-section. **(c-f)** Reproduced under terms of the CC-BY license.[114,116] Copyright 2020 and 2019, The Authors, published by The Optical Society. **g)** Laser annealing of a patterned a-Ge stripe after encapsulation by a silica capping layer. Crystallization starts seeding from the Si substrate below. Reproduced with permission.[118] Copyright 2016, Elsevier.

Along a similar vein, our group has recently demonstrated both laser crystallization and reflowing of pre-patterned a-Si optical waveguides on silica-on-silicon substrates.[114] In contrast to ELA, where typically an entire amorphous thin film is processed,[115] we made use of a CW visible laser to individually process the patterned a-Si waveguides. Scanning of the focused laser beam along the waveguides offered a key advantage in that the laser-induced

heating is highly localized to the patterned waveguide, reducing the power required to melt the smaller material volume and lowering the thermal budget. By optimization of the scan speed to allow for complete melting of the a-Si waveguides, and with the laser power close to the ablation threshold, grain sizes longer than 1 mm were obtained in the longitudinal direction.[116] The transverse grain size can span the entire micron-sized width of the waveguide, thus reducing the number of grain boundaries that the propagating light interacts with. For comparison, large-area CW laser processing without pre-pattering thin films typically results in relatively small grain sizes (2 μm×20 μm) due to difficulties in controlling the crystallization mechanism.[117] Furthermore, as in the case of the processed fins, laser reflowing of the molten Si after patterning enables smooth waveguide surfaces (a root-mean-square roughness of 0.5 nm for our case), which is critical to reduce optical losses due to the surface scattering. As illustrated in Figure 8c,d, the rectangular cross-section of the waveguide transforms into a parabolic shape to minimize the surface tension. As a result, we have obtained poly-Si waveguides with optical losses as low as 4 dB cm^{-1}, which is the lowest loss reported in micron-sized poly-Si waveguides to date. Significantly, this enabled us to observe third-order nonlinear effects, such as two-photon-absorption (TPA)-induced nonlinear losses and self-phase-modulation-induced spectral broadening. The simulated and experimentally captured profiles for a transverse electric (TE) polarized mode are shown in Figure 8e,f, respectively.

Finally, it is worth mentioning that the initial rectangular cross-section can be preserved if the molten material is covered by a silica capping layer, as schematically shown in Figure 8g, where pulsed laser annealing has been used to process a silica-encapsulated a-Ge microstripe on an insulator layer.[118] Moreover, it has recently been demonstrated that a silica cap is necessary to be able to obtain grain-boundary-free lateral crystallization of a-Si thin films on glass substrates, using a fast CW laser scan.[119] Therefore, laser thermal processing of patterned and glass-encapsulated Si waveguides could result in low optical losses similar to those

achieved in SOI platforms and in the Si core glass-clad fibers, but with the prospect of allowing for photonic integration within multi-layered systems built on cheaper, bulk Si platforms.

3.3 Laser-assisted diffusion, alloying and intermixing of semiconductor elements for selective area growth

Complementary to the conventional epitaxial growth methods such as MBE and CVD, selective area heteroepitaxial growth of compound semiconductors can be achieved by deposition through a mask and thermally-assisted diffusion of the deposited elemental semiconductor into the substrate. The best example is the fabrication of graded-index SiGe waveguides within bulk Si wafers. Here, the waveguides are produced by using furnace annealing to in-diffuse Ge from a Ge-rich SiGe strip source deposited on the substrate surface.[120] Although optical losses less than 0.5 dB cm^{-1} were demonstrated at telecom wavelengths (largely due to the excellent Si substrate quality), this approach has not been widely adopted because of the long process times (65 h at 1200 °C) required by the furnace annealing, which renders the fabrication of waveguides impractical.[121] However, UV or visible laser annealing can be used to accelerate the diffusion process for practical fabrication of low-loss diffused waveguides based on compound group IV semiconductors.[122] Selective area growth of a SiGe epilayer via laser-assisted in-diffusion of Ge is schematically shown in **Figure 9a**, where the Ge stripe is deposited via a lift-off process. The width of the diffused region is primarily determined by the photolithography process, while the diffusion depth is controlled by the deposited Ge film thickness and the laser processing parameters. Additionally, the a-Ge strip can be encapsulated by a silica layer to minimize evaporation during in-diffusion. Similarly, growth of GeSn and SiGeSn alloy epilayers have been demonstrated using laser annealing of Sn thin films deposited on Ge-on-Si substrates.[123,124]

Laser processing can also be used to assist constituent mixing after ion implantation for the construction of optoelectronic devices. For example, group IV elements (Ge or Sn) can be implanted within a few hundred nm of the surface to form either patterned or un-patterned

amorphous semiconductor layers, as shown in Figure 9b. Subsequently, pulsed laser melt annealing is used to produce compound semiconductor layers (Figure 9c),[125] recovering ion-implantation-related defects in the crystal structure. Although this works well for the SiGe materials, laser processed GeSn can suffer from Sn phase segregation. However, if short pulses are used, nanosecond or less, the annealing becomes a non-equilibrium process,[126] and it is possible that GeSn alloy epilayers could be produced. Though this will limited by the solid phase solubility limit of Sn, and defects in the crystal structure are also expected to occur due to the relaxation.[127] Nevertheless, selective area fabrication of semiconductor alloy epilayers such as SiGe and GeSn on Si substrates has tremendous implications for active and passive photonic devices, including graded-index waveguides, modulators and lasers, and is thus worth further investigation. Last, but not least, another application of laser thermal annealing is intermixing of elements in multilayer semiconductor heterostructures with digital interfaces, such as multi-quantum wells or superlattices.[128,129] Laser-induced intermixing of Si and Ge in a Si/Ge superlattice is illustrated in Figure 9d. Laser-controlled and selective area intermixing of the quantum well and barrier materials, which is referred to as quantum well intermixing (QWI), provides an alternative route to monolithical fabrication of integrated photonic devices with different bandgaps.

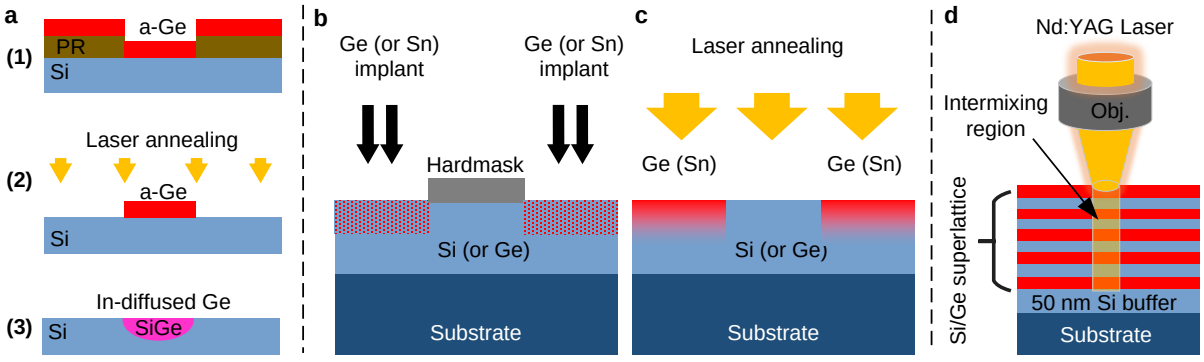

Figure 9. a) Schematic showing Ge in-diffusion by using laser annealing after deposition of a Ge stripe via a lift-off process on a Si substrate. Schematic showing **b)** Sn (Ge) ion implantation into a Ge (Si) substrate and **c)** subsequent laser annealing to obtain on-chip patterned layers of a GeSn (SiGe) alloy. **d)** Laser-induced intermixing of Si and Ge in a Si/Ge superlattice to produce bandgap-shifted regions.

3.4 Laser-driven phase segregation in SiGe alloy thin films with uniform composition

As a reverse of the diffusion processes discussed above, laser processing can also be used to promote phase segregation of the alloy constituents in initially uniform SiGe thin films to produce graded alloy layers or micro-stripe structures, depending on whether the laser is used in static or scanning conditions. However, laser thermal processing of $Si_{1-x}Ge_x$ alloys faces some challenges like constitutional undercooling, which can emerge ahead of the solid/liquid interface when the solidification speed is above a critical value,[23] breaking the stability of the interface. This is particularly restrictive for processing SiGe alloy thin films on glass substrates, because laser thermal annealing of the thin films results in cellular or dendritic structures, leading to a random redistribution of the initially homogenous composition.[130,131] The interface instability in laser-annealed Ge-rich SiGe alloys is even more severe, as the critical speed for stable solidification drops when the Ge content increases.[132] To prevent cellular and dendritic solidification in SiGe thin films, either low solidification speeds or high temperature gradients at the liquid/solid interface must be ensured during directional solidification. However, solidification speeds (<10 μm s^{-1}) for stable growth are too low to be practical in terms of process time. On the other hand, semiconductor alloy thin films grown on substrates with high thermal conductivity, such as bulk Si, allow for achieving extremely high temperature gradients (~10^9 K m^{-1}), which maintain the stability of the solid/liquid interface during solidification.

In the case of large-area static laser exposure of SiGe thin films epitaxially grown on Si substrates using pulsed lasers, the solidification front moves from the film/substrate interface to the top surface in the vertical direction. Due to phase segregation in the laser-melted SiGe film, the shrinking molten region collects more Ge, as the solidification front moves towards the top surface until the entire laser-exposed area solidifies. Therefore, after pulsed laser annealing, initially uniform SiGe thin films transform into compositionally-graded thin films

with a high Ge concentration on the top surface.[133-135] Moreover, the depth of the melted SiGe film and Ge concentration at the top surface can be controlled by the laser fluence. This is quite appealing for applications such as contact resistance lowering in doped SiGe films, and the formation of graded SiGe buffer layers for epitaxial growth of group III-V semiconductor-based photonic devices.

Alternatively, if the laser beam is focused and scanned along the SiGe film surface, we have recently shown that it is possible to fabricate graded-index microstripes, suitable for optical waveguiding applications. In this case the starting film material was amorphous SiGe (a-SiGe) with uniform composition (60% Ge), deposited via PECVD, and the resulting microstripes, which were processed using a 488 nm 0.25 W CW argon-ion laser, were polycrystalline (poly-SiGe), as shown schematically shown in **Figure 10a.**[136] Significantly, by adjusting the scanning speed (0.1-100 mm s^{-1}), it was possible to achieve microstripes with differing Ge concentrations on the top surface, as illustrated by the variation in the color shade (ranging from blue to yellow) in the optical microscope images in Figure 10b. Scanning electron microscopy (SEM) and back-scattered electron detector (BSED) micrographs (Figure 10c-e) show the topography of the surface, and compositional contrast between Ge-rich and Si-rich regions, respectively, as given for scan speeds of 0.1, 10, and 50 mm s^{-1}. The steady-state compositional profiles of the laser-written SiGe microstripes were completely determined by the constant scan speed set before the laser scanning. As this process doesn't require any transient effects such as acceleration or deceleration of the solidification front, indefinitely long $Si_{1-x}Ge_x$ microstripes with scan-speed-dependent composition profiles can be produced.

This work has been complemented with finite-element-method (FEM)-based phase-field simulations to investigate laser-driven phase segregation at different scan speeds. Color maps in Figure 10 f-h show the spatial distribution of the Ge molar fraction x after laser writing at different speeds. The initial Ge molar fraction was $x_0 = 0.6$ mol within the entire volume of the thin film. The laser-induced molten zone (red color) travels along the scan direction

dragging the Ge-rich liquid, which solidifies at the trailing edge. After a Si-rich initial short transient (cyan color), a steady-state region emerges with a Ge-rich strip core and a Si-rich under-cladding. Complete mixing occurs in the molten zone for low scan speeds. However, the Ge content *x* builds up at the trailing edge (darker red) at high scan speeds, due to insufficient diffusion-limited Ge transport. Therefore, the scan speed can be directly used to control the maximum Ge concentration on the surface, as well as the composition distribution within the solidified region. On-chip post-deposition laser writing of semiconductor alloy microstructures with tunable composition profiles could be exploited to fabricate novel devices, including graded-index waveguides,[137-139] multispectral photodetectors, and in-plane heterostructures.

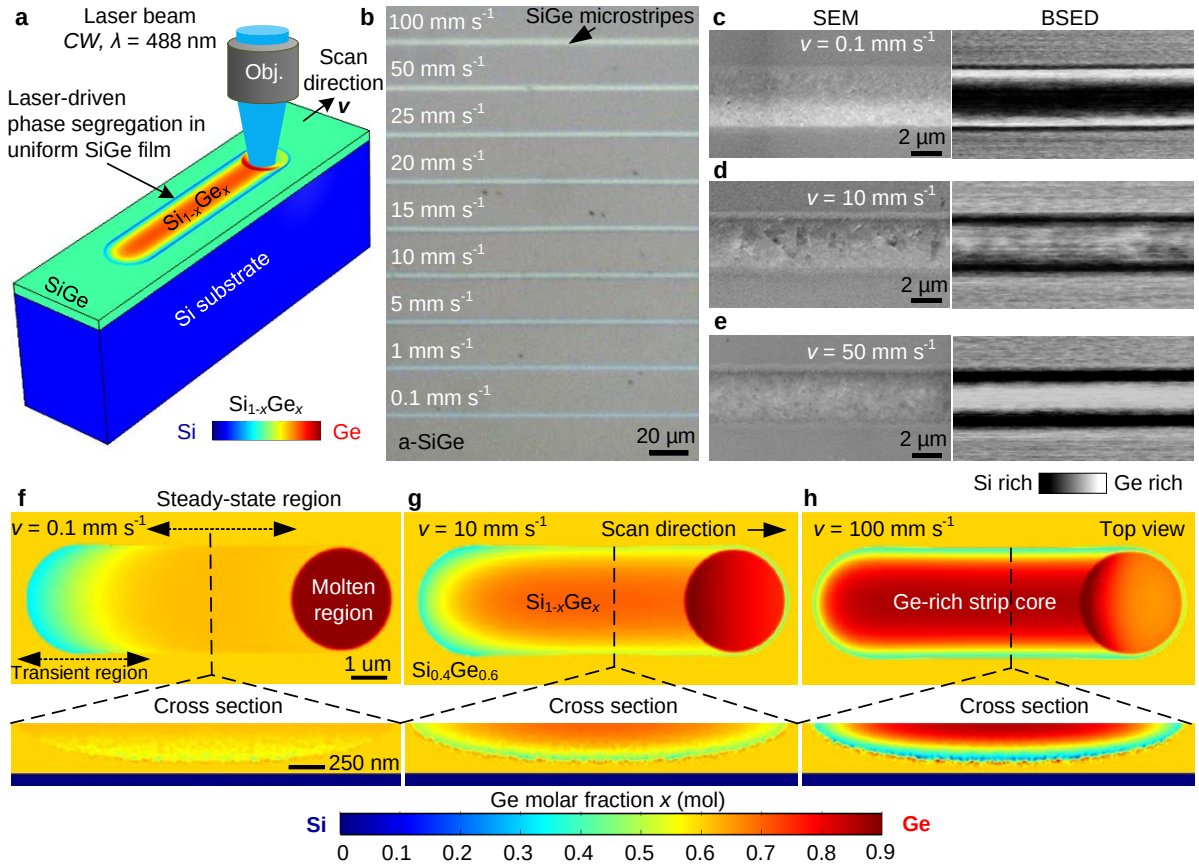

Figure 10. a) Schematic of the laser writing process to achieve scan-speed-dependent phase segregation in an initially homogenous SiGe thin film deposited on a Si substrate. **b)** Optical microscope image showing indefinitely long 3 µm wide laser-written poly-SiGe microstripes with a color shading from blue to yellow depending on the Ge concentration on the top surface. SEM and BSED micrographs show the structural and compositional contrast between Ge-rich (bright) and Si-rich (dark) regions, as given for scan speeds of **c)** 0.1 mm s^{-1}, **d)** 10 mm s^{-1}, and **e)** 50 mm s^{-1}, respectively. Results of FEM-based phase-field simulations, given in color maps, show the spatial distribution of the composition in a SiGe alloy film after laser processing

at scan speeds of **f)** 0.1, **g)** 10, and **h)** 100 mm s^{-1}. **(a-h)** Reprinted with permission.[136] Copyright 2020, American Chemical Society.

3.5 Post-fabrication laser trimming of integrated photonic circuits

Traditional SOI platforms enable the fabrication of highly compact photonic circuits, thanks to the large refractive index difference between the Si core and silica cladding, allowing for strong optical confinement in waveguides. However, high-index-contrast photonic platforms pose fabrication challenges, because the performance of the components are strongly dependent on the waveguide dimensions and any refractive index perturbations, which can be difficult to control at the wafer scale. In particular, resonant and interferometric devices such as micro-ring resonators (MRR)[140] and Mach–Zehnder interferometers (MZI)[141] are highly sensitive to the variations of the effective mode index and phase, respectively. This can lead to poor device performance if there is any variation from the original design. Therefore, it is imperative to be able to compensate for fabrication tolerances and to tune individual components within integrated photonic circuits, even when the most advanced fabrication tools such as e-beam lithography are used. To date, various active trimming methods have been developed. For example, photonic components can be actively tuned by micro-heaters[142] and charge carrier injections through p-n junctions,[143] using thermo-optic and free-carrier dispersion (FCD) effects. However, the layout design becomes increasingly complex and power consumption can be prohibitive for hundreds of devices integrated on the same wafer. As an alternative approach, post-fabrication trimming methods have been investigated to permanently modify the refractive index of either the waveguide core or the cladding material through various laser-assisted processes including oxidation,[144] dehydrogenization,[145] and annealing.[140]

One of the post-fabrication trimming methods attracting considerable attention over the past decade is laser annealing of ion-implanted silicon photonic devices, such as MRRs[146] and MZIs.[141] Ge ion implantation is particularly promising as it is CMOS compatible and isoelectronic to Si, hence doesn’t cause any unintentional doping. Moreover, due to the large

atomic radius of Ge compared to other ion sources, it allows for amorphization of the Si lattice at relatively low implantation doses (~10^{15} Ge-ions cm^{-2}), at room temperatures. Ge-implanted Si has a refractive index *n* of 3.96,[147] which can be gradually reduced to that of initial c-Si (n_{si}=3.46) by restoration of the crystal structure through limited laser-induced crystallization. This process can be controlled by the laser power, scan speed, and length of the annealed section in the Ge-implanted region. For rib waveguide structures, either the core or the cladding slab can be implanted, which allows for direct modulation of the core guided light or modification of the coupling region between different components, such as a bus waveguide and resonator as schematically shown in **Figure 11a**. Using pulsed laser annealing of the Ge-implanted stripe (Figure 11b), both the resonant wavelengths and the critical coupling condition of the racetrack resonator could be tuned post-fabrication,[148] as shown in the transmission spectra before and after laser trimming (Figure 11c). Ge implantation was also used to produce 1000 μm long Bragg grating reflectors in Si waveguides with extinction ratios up to 25 dB.[147] The Bragg grating reflectors, which consist of Ge-implanted a-Si regions with a period of 212 nm, were selectively removed by UV pulsed laser annealing, and the original flat transmission of the waveguides were recovered.

CW laser annealing is another post-fabrication trimming tool, which can be applied to photonic components based on Ge-implanted silicon. Compared to pulsed laser annealing,[148] it can perform better at removing residual absorption losses as it is capable of producing larger grain sizes with fewer defects after crystallization, due to the lower cooling rates. By using a 488 nm CW Argon ion laser set to a power of 0.18 W, Topley et al.[149] demonstrated erasing of a Ge-implanted vertical grating coupler, which can be used to couple light into and out from a waveguide at an arbitrary point along the optical circuit. After laser annealing, the output coupling efficiency drops by 21 dB, while the transmission through the annealed regions increases by 5.7 dB compared to the grating transmission before laser annealing. Laser-erasable vertical grating couplers enable in situ measuring of single-pass transmission characteristics at

the individual component level in integrated photonics systems, hence allowing for early detection of devices with poor performance or failure.

Additionally, CW laser annealing has been used by Chen et al.[150] to trim the operational point of a directional coupler (DC), shown in Figure 11d. Step by step transverse raster scanning of the laser beam (Figure 11e) allows for precise selective annealing of the Ge-implanted stripe (red). The transmission spectra of the drop and through ports as a function of the length of the laser-annealed section are given in Figure 11f. Ge-implanted components in integrated silicon photonic systems,[150] which are either erasable (waveguides) or tunable (MZI, MRR, and DC) by post-fabrication laser annealing, offer an on-demand non-volatile configurability, which can be used to permanently switch optical signals among different ports and perform various functions. Thus this application of laser processing opens up a new era for programmable multi-purpose photonic circuits.

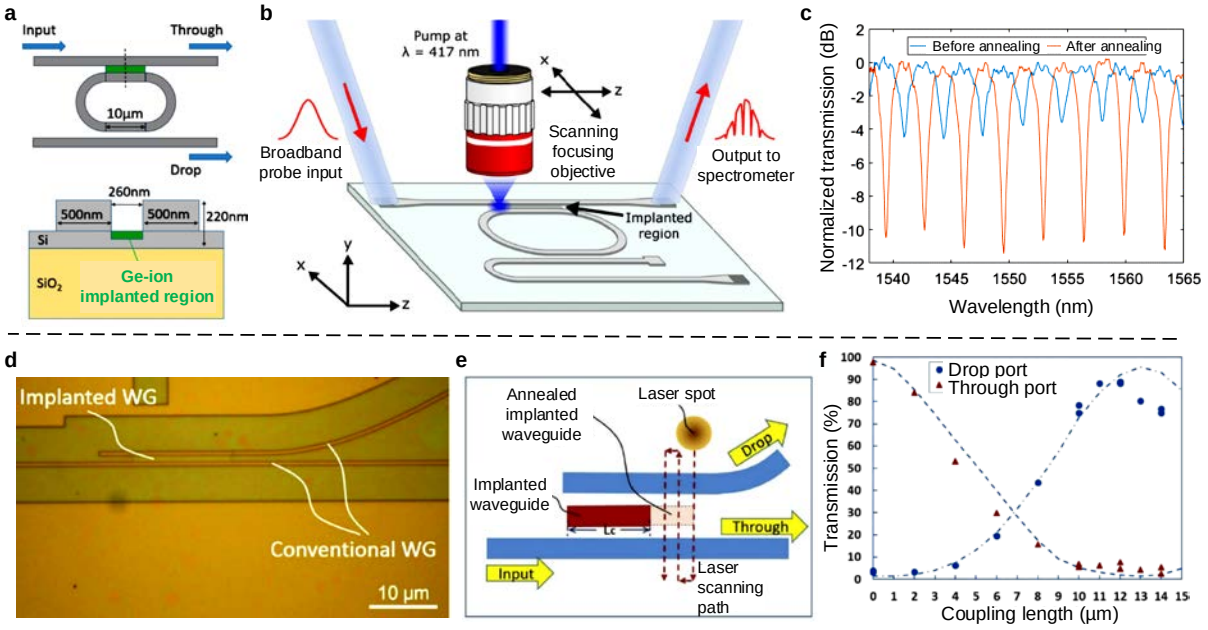

Figure 11. a) Schematics showing Ge-implanted regions (green) in top and cross-section views. **b)** Laser trimming of critical coupling in a racetrack resonator by thermal annealing of the Ge-implanted stripe using a 417 nm pulsed laser. **c)** Transmission spectrum of the race-track resonator before and after laser trimming. **(a-c)** Reproduced under terms of the CC-BY license.[148] Copyright 2020, The Authors, published by IEEE. **d)** Optical microscope image showing a directional coupler that consists of two Si waveguides and a Ge-implanted stripe between them. **e)** Schematic showing laser annealing of the Ge-implanted stripe using transverse raster scan. **f)** Transmission spectra of the drop and through ports versus the length

of the laser-annealed section in the Ge-implanted stripe. **(d-f)** Reproduced under terms of the CC-BY license.[150] Copyright 2020, The Authors, published by The Optical Society.

3.6 Surface nanostructures via laser-induced phase and morphological transformations

The prospect of CMOS-compatible configurable meta-surfaces has stimulated intense research efforts in the fabrication of ordered Si nanostructures with sub-wavelength features.[151] Si-based dielectric nanostructures present opportunities similar to metallic nanostructures in terms of their optical response, which can be tuned by geometry. However, Si offers additional benefits due to its high refractive index and low absorption in the telecom wavelength band. Furthermore, reversible transformations between amorphous and crystalline phases can be induced in isolated geometries by pulsed laser annealing, enabling applications such as structural coloring, dynamic wave-front control, and so forth. **Figure 12a** shows a photonic device consisting of 30 nm thick a-Si nano-disk arrays deposited and patterned on a silica substrate, functioning as a pixelated surface, which modulates the wave-front of a read/probe laser.[152] Each pixel can be addressed by a 532 nm pulsed laser to either crystallize or amorphize the Si nano-disks, using 13 nanosecond pulses, but with different fluences. A fluence of 1.8 J cm^{-2} was shown to deposit sufficient energy to transform an a-Si nano-disk into a c-Si nano-disk. However, a higher fluence of 2.1 J cm^{-2} melted the c-Si disk entirely down to the silica substrate, resulting in transformation back to the amorphous phase after quenching. Figure 12b illustrates the phase transformation cycle, where the intermediate state is liquid Si (l-Si). The a-Si (red) and c-Si (green) display different colors in bright-field optical microscopy, due to the shift in the Mie resonances in the visible spectrum. The phase transformation allows for a nonvolatile 20% change in the reflectivity. Two different laser-written Fresnel zone plates (FZPs), which are based on the reconfigurable pixelated meta-surface, are shown in Figure 12c. The diameter and pitch of the Si nano-disks in the FZPs are 215 nm and 550 nm, respectively. The FZPs have been demonstrated to possess focal points of 353 μm and 207 μm by measuring

the intensity distribution in the cross-section at different distances in the normal direction (Figure 12d).

Self-organized nanostructures can also be directly induced on the surface of almost any material, including semiconductors, by laser processing with single as well as dual beams. This universal phenomenon is known as laser-induced periodic surface structures (LIPSS), which emerge as periodic surface protrusions and depressions upon laser radiation.[153] By using different laser types, optical powers, number of laser beams, and processing conditions, various LIPSS have been demonstrated to date, with control over the length, height, and direction of the nanostructures, as well as their periods, which can be smaller than the diffraction limit or larger than the wavelength. Depending on the laser processing parameters and material, LIPPS originate from electromagnetic effects such as the interference of the incident and surface scattered beams, or matter organization due to thermocapillary effects.[154]

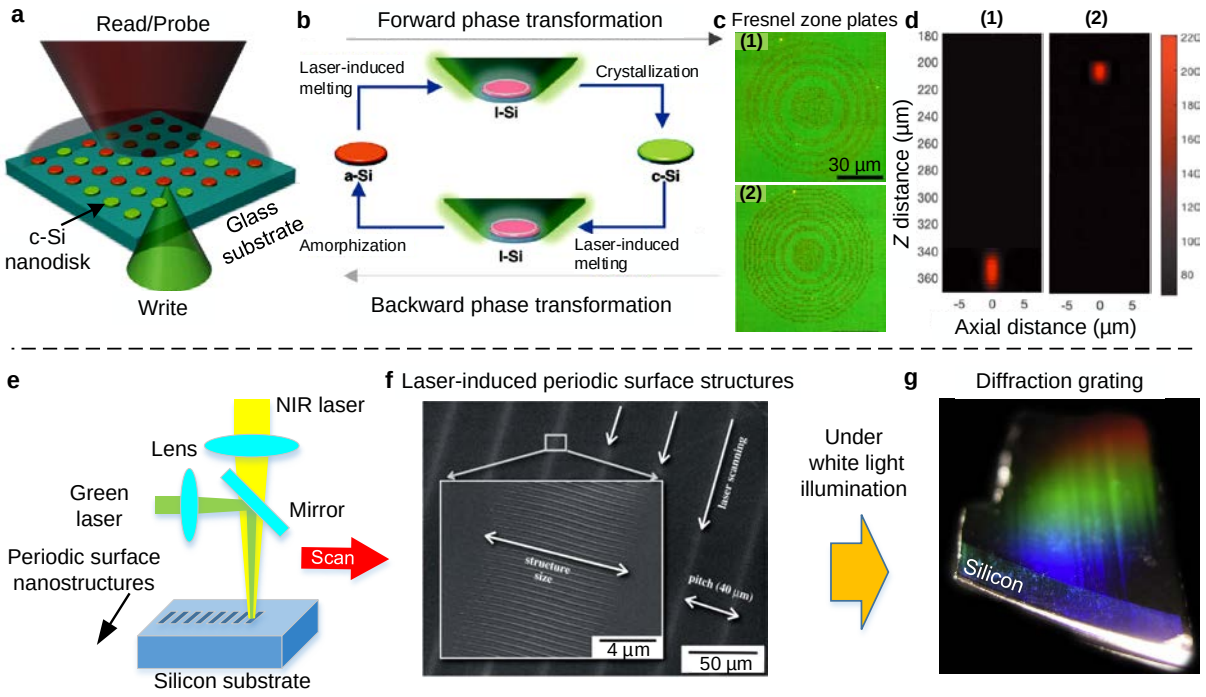

Figure 12. a) Schematic showing a pixel-addressable rewritable visible meta-surface that consists of arrays of Si nano-disks on a silica substrate, where each can be transformed into crystal or amorphous phases by pulsed laser annealing. **b)** Phase transformation cycle controlled by laser-induced melting with 13 ns pulses at different fluences. **c,d)** Two different laser-written Fresnel zone plates with on-demand modification with corresponding focal points in **(d)**. **(a-d)** Reproduced with permission.[152] Copyright 2020, Wiley-VCH Verlag GmbH & Co. KGaA, Weinheim. **e)** Schematic showing writing of periodic surface structures using two CW lasers

on a Si substrate amorphized by ion-implantation. **f)** SEM micrograph showing laser-written microstripes with periodic nanostructures, which can be used as **g)** a large-area visible diffraction grating. **(f,g)** Reproduced with permission.[155] Copyright 2011, IOP Publishing Ltd.

LIPSS on a Si surface, which was amorphized down to a depth of 250 nm by ion implantation, was demonstrated by using a 532 nm CW laser and a 797 nm CW NIR laser,[155] as schematically shown in Figure 12e. The dual laser processing resulted in nano-stripe grating lines (Figure 12f) with periods adjustable in the range 530-800 nm by controlling the power of the green laser (12-18 W), while keeping the power of the NIR laser constant. The direction of the nano-stripes is perpendicular to the polarization of the beam, which is along the laser scanning. One application of these periodic nanostructures on Si substrates is diffraction gratings in the visible spectrum (Figure 12g). Similar periodic nanostructures have been produced on SiGe thin films epitaxially grown on Si substrates by using a 248 nm excimer laser with a pulse duration of 25 ns.[156] Both periodic ripples and self-organized cone-like protrusions have been produced using different power levels. It is worth to note that the surface modulation on SiGe thin films can couple to the composition modulation at high power levels.[157]

3.7 Future prospects

As we have seen, there are already numerous applications for laser processing of planar semiconductor components and circuits of use for photonic applications. Here we outline some potential directions for further development.

3.7.1 Fabrication of photonic components on bulk silicon incorporating laser processing

Bulk Si wafers are likely to be used in the future for integration of electronic/photonic circuits, due to the lower cost and superior heat dissipation compared to SOI platforms. Therefore, there is a strong desire to establish efficient fabrication methods for photonic components on such wafers. For optical isolation of the waveguides, local buried oxide layers have been used under poly-Si waveguides crystallized using heat treatments. Capitalizing on our recent work,[114] we expect that laser annealing of patterned and glass-encapsulated a-Si waveguides can provide

better results in terms of crystallinity, enabling the optical losses close to those of c-Si waveguides. On the other hand, modification of the material properties via nonlinear multiphoton effects using ultrafast lasers presents an etch-free maskless approach for fabrication optical waveguides with optical losses as low as 2.2 dB cm^{-1} within bulk Si.[158,159] Another approach would be using SiGe epilayers grown on bulk Si and direct CW laser writing to produce graded-index waveguides via phase segregation. Last, but not least, laser-induced surface nanostructures could be used as both vertical grating optical couplers and Bragg grating reflectors, if fabricated on conventional optical waveguides.

3.7.2 Fabrication of Sn-based active devices using pulsed laser annealing

In recent years, $Ge_{1-x}Sn_x$ alloys have attracted great interest for the fabrication of CMOS-compatible optoelectronic devices such as photodetectors, light emitting diodes and lasers,[64-66] because alloying Ge with 8 at.% Sn in an unstrained state allows for a true direct electronic bandgap material. Therefore, various epitaxial growth methods have been developed to grow GeSn alloy thin films on Si substrates.[160] However, these methods suffer from i) the low equilibrium solid solubility of Sn in Ge, ii) segregation of Sn on the surface at high deposition temperatures, and iii) a large lattice mismatch (>4%) between $Ge_{1-x}Sn_x$ and Si. On the other hand, complementary to the meta-stability via direct epitaxy, non-equilibrium regrowth could be achieved by nanosecond (and shorter) pulsed laser annealing of either amorphous GeSn thin films or Sn-implanted Ge thin films on substrates with high thermal conductivities, as recently demonstrated.[127] Furthermore, laser thermal processing generally results in residual tensile strains in semiconductor thin films on Si substrates, which may assist in obtaining a direct bandgap for low Sn content GeSn alloys.[161] However, despite these prospects, laser-processed GeSn thin films have yet to be used for fabrication of active photonic devices, due to the ongoing challenges such as high Sn segregation and constitutional supercooling, leading to cellular breakdown.

3.7.3 Laser-written in-plane periodic heterostructures in semiconductor alloy epilayers

Transient effects such as acceleration or deceleration of the liquid/solid interface during directional solidification can be used to produce localized compositional heterostructures in binary alloys. Grating-like periodic compositional structures have been already demonstrated in SiGe core fibers, by periodic modulation of the laser power and scan speed during laser processing,[23] as covered in **Section 2.4**. However, this has yet to be demonstrated in semiconductor alloy epilayers on planar substrates. We anticipate that in-plane transverse heterostructures and superlattices could be fabricated in SiGe epilayers grown on Si substrates by controlling phase segregation through modulation of the laser power, scan speed and beam position during directional solidification.[162] This would be complementary to vertical heterostructure formation via epitaxial growth on planar substrates layer by layer using convectional deposition methods (MBE, CVD). Post-deposition laser writing of periodic nanoscale heterostructures in the plane of semiconductor alloy epilayers by modulation of laser processing parameters could pave the way for new device applications in the fields of optoelectronics and photonics such as waveguide Bragg gratings and multi-quantum-wire lasers.

4. Conclusion

This paper has reviewed some of the key applications of laser thermal processing of group IV semiconductors and their compounds used for the fabrication of integrated photonic systems, including both fiber and planar platforms. We note that our focus here has been on thermal processing induced by the optical absorption of laser radiation, excluding nonlinear multi-photon effects and ablation induced by ultrafast lasers (sub-ps). In this sense, this review is complementary to the existing reviews that cover application of ultrafast lasers for patterning, deposition, and machining of materials in general.[14, 16,163-168] More historical progress for laser annealing of ion-implanted semiconductors are given in Refs.[169-171]

By applying laser thermal processing to the semiconductor core fibers, it is possible not only to produce fibers with monocrystalline core materials with the lowest optical losses of this fiber class, but also to engineer the bandgap, composition, structure, and morphology of these

cores. Thus these results are of great technological importance in the quest to realize fully integrated multi-material and multi-functional fiber-based photonic and optoelectronic systems. For the planar photonic devices, in addition to enhancing the structural and optical properties of waveguides fabricated from deposited materials, laser processing can also be used for the direct writing of waveguides and photonic meta-surfaces in semiconductor thin films, as well as for programming of general-purpose integrated photonic circuits to perform various functions. In addition to highlighting the current state-of-the-art and existing challenges facing laser processing of semiconductor materials, this review also sets out some exciting future prospects for the field. We hope that it will serve to stimulate new avenues for experimental exploitation of laser processing as a multipurpose powerful tool, and contribute to the future fabrication of integrated group IV photonic systems.[172]

Acknowledgments

The authors acknowledge the support of the Engineering and Physical Sciences Research Council (EPSRC) (EP/P000940/1, EP/N013247/1 and EP/M022757/1).

Conflict of Interests

The authors declare no conflict of interests.

Received: ((will be filled in by the editorial staff))
Revised: ((will be filled in by the editorial staff))
Published online: ((will be filled in by the editorial staff))

References

[1] W. N. Ye, Y. Xiong, *J. Mod. Opt.* **2013**, *60*, 1299.

[2] X. Chen, M. M. Milosevic, S. Stanković, S. Reynolds, T. D. Bucio, K. Li, D. J. Thomson, F. Gardes, G. T. Reed, *Proc. IEEE* **2018**, *106*, 2101.

[3] P. Dong, Y.-K. Chen, G.-H. Duan, D. T. Neilson, *Nanophotonics* **2014**, *3*, 215.

[4] Y. Ishikawa, K. Wada, *Thin Solid Films* **2010**, *518*, S83.

[5] W. Bogaerts, D. Taillaert, B. Luyssaert, P. Dumon, J. Van Campenhout, P. Bienstman, D. Van Thourhout, R. Baets, *Opt. Express* **2004**, *12*, 1583.

[6] C. Sun, M. T. Wade, Y. Lee, J. S. Orcutt, L. Alloatti, M. S. Georgas, A. S. Waterman, J. M. Shainline, R. R. Avizienis, S. Lin, B. R. Moss, R. Kumar, F. Pavanello, A. H. Atabaki, H. M.

Cook, A. J. Ou, J. C. Leu, Y.-H. Chen, K. Asanović, R. J. Ram, M. A. Popović, V. M. Stojanović, *Nature* **2015**, *528*, 534.

[7] R. S. Jacobsen, K. N. Andersen, P. I. Borel, J. Fage-Pedersen, L. H. Frandsen, O. Hansen, M. Kristensen, A. V. Lavrinenko, G. Moulin, H. Ou, C. Peucheret, B. Zsigri, A, Bjarklev, *Nature* **2006**, *441*, 199.

[8] R. Geiger, T. Zabel, H. Sigg, *Front. Mater.* **2015**, *2*, 52.

[9] R. Soref, D. Buca, S.-Q. Yu, *Opt. Photonics News* **2016**, *27*, 32.

[10] A. H. Atabaki, S. Moazeni, F. Pavanello, H. Gevorgyan, J. Notaros, L. Alloatti, M. T. Wade, C. Sun, S. A. Kruger, H. Meng, K. Al Qubaisi, I. Wang, B. Zhang, A. Khilo, C. V. Baiocco, M. A. Popović, V. M. Stojanović, R. J. Ram, *Nature* **2018**, *556*, 349.

[11] K. Preston, B. Schmidt, M. Lipson, *Opt. Express* **2007**, *15*, 17283.

[12] L. Rebohle, S. Prucnal, W. Skorupa, *Semicond. Sci. Technol.* **2016**, *31*, 103001.

[13] J. D. Majumdar, I. Manna, *Int. Mater. Rev.* **2011**, *56*, 341.

[14] N. A. Vainos, in *Laser growth and processing of photonic devices*, (Ed: N. A. Vainos), Woodhead Publishing Limited, Cambridge, UK 2012, Ch. 1.

[15] R. T. Young, R. F. Wood, *Ann. Rev. Mater. Sci.* **1982**, *12*, 323.

[16] J. C. Ion, *Laser Processing of Engineering Materials: Principles, Procedure and Industrial Application*, Elsevier Butterworth-Heinemann, Oxford, UK **2005**.

[17] A. C. Peacock, J. Campling, A. F. J. Runge, H. Ren, L. Shen, O. Aktas, P. Horak, N. Healy, U. J. Gibson, J. Ballato, *IEEE J. Sel. Top. Quantum Electron.* **2018**, *24*, 5100309.

[18] P. Mehta, N. Healy, T. D. Day, J. R. Sparks, P. J. A. Sazio, J. V. Badding, A. C. Peacock, *Opt. Express* **2011**, *19*, 19078.

[19] K. Sui, X. Feng, Y. Hou, Q. Zhang, S. Qi, Y. Wang, P. Wang, *Opt. Mater. Express* **2017**, *7*, 1211.

[20] J. Ballato, T. Hawkins, P. Foy, R. Stolen, B. Kokuoz, M. Ellison, C. McMillen, J. Reppert, A. M. Rao, M. Daw, S. Sharma, R. Shori, O. Stafsudd, R. R. Rice, D. R. Powers, *Opt. Express* **2008**, *16*, 18675.

[21] J. Ballato, T. Hawkins, P. Foy, B. Yazgan-Kokuoz, R. Stolen, C. McMillen, N. K. Hon, B. Jalali, R. Rice, *Opt. Express* **2009**, *17*, 8029.

[22] D. Homa, Y. Liang, C. Hill, G. Kaur, G. Pickrell, *Appl. Phys. A* **2015**, *118*, 23.

[23] D. A. Coucheron, M. Fokine, N. Patil, D. W. Breiby, O. T. Buset, N. Healy, A. C. Peacock, T. Hawkins, M. Jones, J. Ballato, U. J. Gibson, *Nat. Commun.* **2016**, *7*, 13265.

[24] J. Zhang, T. Zhang, H. Zhang, Z. Wang, C. Li, Z. Wang, K. Li, X. Huang, M. Chen, Z. Chen, Z. Tian, H. Chen, L.-D. Zhao, L. Wei, *Adv. Mater.* **2020**, *32*, 2002702.

[25] N. Healy, U. Gibson, A. C. Peacock, *Semicond. Sci. Technol.* **2018**, *33*, 023001.

[26] A. C. Peacock, U. J. Gibson, J. Ballato, *Adv. Phys.: X* **2016**, *1*, 114.

[27] A. C. Peacock, N. Healy, *Semicond. Sci. Technol.* **2016**, *31*, 103004.

[28] J. R. Sparks, P. J. A. Sazio, V. Gopalan, J. V. Badding, *Annu. Rev. Mater. Res.* **2013**, *43*, 527.

[29] S. Chaudhuri, J. R. Sparks, X. Ji, M. Krishnamurthi, L. Shen, N. Healy, A. C. Peacock, V, Gopalan, J V. Badding, *ACS Photonics* **2016**, *3*, 378.

[30] P. J. A. Sazio, A. Amezcua-Correa, C. E. Finlayson, J. R. Hayes, T. J. Scheidemantel, N. F. Baril, B. R. Jackson, D.-J. Won, F. Zhang, E. R. Margine, V. Gopalan, V. H. Crespi, J. V. Badding, *Science* **2006**, *311*, 1583.

[31] P. Mehta, M. Krishnamurthi, N. Healy, N. F. Baril, J. R. Sparks, P. J. A. Sazio, V. Gopalan, J. V. Badding, A. C. Peacock, *Appl. Phys. Lett.* **2010**, *97*, 071117.

[32] J. Ballato, A. C. Peacock, *APL Photonics* **2018**, *3*, 120903.

[33] J. Ballato, T. Hawkin, P. Foy, S. Morris, N. K. Hon, B. Jalali, R. Rice, *Opt. Express* **2011**, *36*, 687.

[34] D. Wang, N. Chen, Z. Chen, Z. Zhao, F. Pang, T. Wang, *AIP Advances* **2018**, *8*, 065006.

[35] H. El Hamzaoui, G. Bouwmans, B. Capoen, N. Chen, M. Douay, M. Bouazaoui, *Mater. Today Commun.* **2017**, *11*, 179.

[36] W. Zhang, N. Chen, Z. Chen, Z. Zhao, Q. Guo, F. Pang, T. Wang, *IOP Conf. Series: Journal of Physics: Conf. Series* **2017**, *844*, 012058.

[37] Y. Franz, A. F. J. Runge, H. Ren, N. Healy, K. Ignatyev, M. Jones, T. Hawkins, J. Ballato, U. J. Gibson, A. C. Peacock, *Opt. Mater. Express* **2017**, *7*, 2055.

[38] E. F. Nordstrand, A. N. Dibbs, A. J. Eraker, U. J. Gibson, *Opt. Mater. Express* **2013**, *3*, 651.

[39] H. Ren, L. Shen, D. Wu, O. Aktas, T. Hawkins, J. Ballato, U. J. Gibson, A. C. Peacock, *Opt. Mater. Express* **2019**, *9*, 1271.

[40] G. Tao, H. Ebendorff-Heidepriem, A. M. Stolyarov, S. Danto, J. V. Badding, Y Fink, J. Ballato, A. F. Abouraddy, *Adv. Opt. Photonics* **2015**, *7*, 379.

[41] H. K. Tyagi, M. A. Schmidt, L. P. Sempere, P. St.J. Russell, Opt. Express **2008**, *16*, 17227.

[42] H. Chen, S. Fan, G. Li, M A. Schmidt, N. Healy, *IEEE Photonics Technol. Lett.* **2020**, *32*, 81.

[43] X. Ji, S. Lei, S.-Y. Yu, H. Y. Cheng, W. Liu, N. Poilvert, Y. Xiong, I. Dabo, S. E. Mohney, J. V. Badding, *ACS Photonics* **2017**, *4*, 85.

[44] X. Ji, R. L. Page, S. Chaudhuri, W. Liu, S.-Y. Yu, S. E. Mohney, J. V. Badding, V. Gopalan, *Adv. Opt. Mater.* **2017**, *5*, 1600592.

[45] N. Healy, M. Fokine, Y. Franz, T. Hawkins, M. Jones, J. Ballato, A. C. Peacock, U. J. Gibson, *Adv. Optical Mater.* **2016**, *4*, 1004.

[46] Z. Zhao, Y. Mao, L. Ren, J. Zhang, N. Chen, T. Wang, *Opt. Mater. Express* **2019**, *9*, 1333.

[47] N. Healy, S. Mailis, N. M. Bulgakova, P. J. A. Sazio, T. D. Day, J. R. Sparks, H. Y. Cheng, J. V. Badding, A. C. Peacock, *Nat. Mater.* **2014**, *13*, 1122.

[48] I. Avrutsky, R. Soref, *Opt. Express* **2011**, *19*, 21707.

[49] R. S. Jacobsen, K. N. Andersen, P. I. Borel, J. Fage-Pedersen, L. H. Frandsen, O. Hansen, M. Kristensen, A. V. Lavrinenko, G. Moulin, H. Ou, C. Peucheret, B. Zsigri, A. Bjarklev, *Nature* **2006**, *441*, 199.

[50] M. Fokine, A. Theodosiou, S. Song, T. Hawkins, J. Ballato, K. Kalli, U. J. Gibson, *Opt. Mater. Express* **2017**, *7*, 1589.

[51] G. G. Pethuraja, R. E. Welser, A. K. Sood, C. Lee, N. J. Alexander, H. Efstathiadis, P. Haldar, J. L. Harvey, *Mater. Sci. Appl.* **2012**, *3*, 67.

[52] R. W. Olensinski, G. J. Abbaschian, *Bull. Alloy Phase Diagrams* **1984**, *5*, 180.

[53] W. Wu, M. H. Balci, K. Mühlberger, M. Fokine, F. Laurell, T. Hawkins, J. Ballato, U. J. Gibson, *Opt. Mater. Express* **2019**, *9*, 4301.

[54] W. Wu, M. Balci, S. Song, C. Liu, M. Fokine, F. Laurell, T. Hawkins, J. Ballato, U. J. Gibson, *Opt. Mater. Express* **2020**, *10*, 926.

[55] S. Song, K. Lønsethagen, F. Laurell, T. W. Hawkins, J. Ballato, M. Fokine, U.J. Gibson, *Nat. Commun.* **2019**, *10*, 1790.

[56] J. J. Kaufman, G. Tao, S. Shabahang, E.-H. Banaei, D. S. Deng, X. Liang, S. G. Johnson, Y. Fink, A. F. Abouraddy, *Nature* **2012**, *487*, 463.

[57] C. F. de Lima, L. A. van der Elst, V. N Koraganji, M. Zheng, M. G. Kurtoglu, A. Gumennik, *Nanoscale Res. Lett.* **2019**, *14*, 209.

[58] J. Zhang, Z. Wang, Z. Wang, T. Zhang, L. Wei, *ACS Appl. Mater. Interfaces* **2019**, *11*, 45330.

[59] O. Aktas, E. Ozgur, O. Tobail, M. Kanik, E. Huseyinoglu, M. Bayindir, *Adv. Opt. Mater.* **2014**, *2*, 618.

[60] A. Gumennik, L. Wei, G. Lestoquoy, A. M. Stolyarov, X. Jia, P. H. Rekemeyer, M. J. Smith, X. Liang, B. J.-B. Grena, S. G. Johnson, S. Gradećak, A. F. Abouraddy, J. D. Joannopoulos, Y. Fink, *Nat. Commun.* **2013**, *4*, 2216.

[61] J. Zhang, K. Li, T. Zhang, P. J. S. Buenconsejo, M. Chen, Z. Wang, M. Zhang, Z. Wang, L. Wei, *Adv. Funct. Mater.* **2017**, *27*, 1703245.

[62] A. Gumennik, E. C. Levy, B. Grena, C. Hou, M. Rein, A. F. Abouraddy, J. D. Joannopoulos, Y. Fink, *Proc. Natl. Acad. Sci. U. S. A.* **2017**, *114*, 7240.

[63] J. Zhang, Z. Wang, Z. Wang, T. Zhang, L. Wei, *Nat. Commun.* **2019**, *10*, 5206.

[64] S. Ghosh, K.-C. Lin, C.-H. Tsai, H. Kumar, Q. Chen, L. Zhang, B. Son, C. S. Tan, M. Kim, B. Mukhopadhyay, G.-E. Chang, *Micromachines* **2020**, *11*, 795.

[65] B.-J. Huang, C.-Y. Chang, Y.-D. Hsieh, R. A. Soref, G. Sun, H.-H. Cheng, G.-E. Chang, *ACS Photonics* **2019**, *6*, 1931.

[66] Y. Zhou, W. Dou, W. Du, S. Ojo, H. Tran, S. A. Ghetmiri, J. Liu, G. Sun, R. Soref, J. Margetis, J. Tolle, B. Li, Z. Chen, M. Mortazavi, S.-Q. Yu, ACS Photonics **2019**, *6*, 1434.

[67] J. Shi, F. Han, C. Cui, Y. Yu, X. Feng, *Opt. Commun.* **2020**, *459*, 125093.

[68] A. Sandupatla, J. Flattery, P. Kornreich, *Opt. Eng.* **2015**, *54*, 126113.

[69] S. Morris, T. Hawkins, P. Foy, C. McMillen, J. Fan, L. Zhu, R. Stolen, R. Rice, J. Ballato, *Opt. Express* **2011**, *1*, 1141.

[70] C. Hou, X. Jia, L. Wei, S-C Tan, X. Zhao, J. D. Joannopoulos, Y. Fink, *Nat. Commun.* **2015**, *6*, 6248.

[71] Y. P. Huang, L. A. Wang, *Appl. Phys. Lett.* **2015**, *106*, 191106.

[72] J.-H. Chen, Y.-T. Sun, L. A. Wang, *IEEE Photonics Technol. Lett.* **2016**, *28*, 1774.

[73] H. Ren, O. Aktas, Y. Franz, A. F. J. Runge, T. Hawkins, J. Ballato, U. J. Gibson, A. C. Peacock, *Opt. Express* **2017**, *25*, 24157.

[74] S. Saito, F. Y. Gardes, A. Z. Al-Attili, K. Tani, K. Oda, Y. Suwa, T. Ido, Y. Ishikawa, S. Kako, S. Iwamoto, Y. Arakawa, *Front. Mater.* **2014**, *1*, 15.

[75] G. Z. Mashanovich, M. Nedeljkovic, J. Soler-Penades, Z. Qu, W. Cao, A. Osman, Y. Wu, C. J. Stirling, Y. Qi, Y. Xu-Cheng, L. Reid, C. G. Littlejohns, J. Kang, Z. Zhao, M. Takenaka, T. Li, Z. Zhou, F. Y. Gardes, D. J. Thomson, G. T. Reed, *Opt. Mater. Express* **2018**, *8*, 2276.

[76] L. Zhang, A. M. Agarwal, L. C. Kimerling, J. Michel, *Nanophotonics* **2014**, *3*, 247.

[77] S. Wirths, D. Buca, S. Mantl, *Prog. Cryst. Growth Charact. Mater.* **2016**, *62*, 1.

[78] S. Zaima, O. Nakatsuka, N. Taoka, M. Kurosawa, W. Takeuchi, M. Sakashita, *Sci. Technol. Adv. Mater.* **2015**, *16*, 043502.

[79] J. Liu, *Photonics* **2014**, *1*, 162.

[80] D. J. Paul, *Semicond. Sci. Technol.* **2004**, *19*, R75.

[81] P. Chaisakul, V. Vakarin, J. Frigerio, D. Chrastina, G. Isella, L. Vivien, D. Marris-Morini, *Photonics* **2019**, *6*, 24.

[82] Y. Yamamoto, O. Skibitzki, M. A. Schubert, M. Scuderi, F. Reichmann, M. H. Zöllner, M. De Seta, G. Capellini, B. Tillack, *Jpn. J. Appl. Phys.* **2020**, *59*, SGGK10.

[83] M. Oehme, D. Widmann, K. Kostecki, P. Zaumseil, B. Schwartz, M. Gollhofer, R. Koerner, S. Bechler, M. Kittler, E. Kasper, J. Schulze, *Opt. Lett.* **2014**, *39*, 4711.

[84] O. O. Abegunde, E. T. Akinlabi, O. P. Oladijo, S. Akinlabi, A. U. Ude, *AIMS Mater. Sci.* **2019**, *6*, 174.

[85] M. Oehme, J. Werner, O. Kirfel, E. Kasper, *Appl. Surf. Sci.* **2008**, *254*, 6238.

[86] R. J. Martin-Palma, A. Lakhtakia, in *Engineered Biomimicry*, (Eds: R. J. Martin-Palma, A. Lakhtakia), Elsevier, USA **2013**, Ch. 15.

[87] J. Murota, M. Sakuraba, B. Tillack, *Jpn. J. Appl. Phys.* **2006**, *45*, 6767.

[88] M. Moravej, S. E. Babayan, G. R. Nowling, X. Yang, R. F. Hicks, *Plasma Sources Sci. Technol.* **2004**, *13*, 8.

[89] B. Claflin, G. J. Grzybowski, M. E. Ware, S. Zollner, A. M. Kiefer, *Front. Mater.* **2020**, *7*, 44.

[90] G. Dushaq, M. Rasras, A. Nayfeh, *Thin Solid Films* **2017**, *636*, 585.

[91] S. Z. Oo, A. Tarazona, A. Z. Khokhar, R. Petra, Y. Franz, G. Z. Mashanovich, G. T. Reed, A. C. Peacock, H. M. H. Chong, *Photonics Res.* **2019**, *7*, 193.

[92] T. Lipka, L. Moldenhauer, J. Müller, H. K. Trieu, *Photonics Res.* **2016**, *4*, 126.

[93] D. K. Rai, C. S. Solanki, B. R. Kavaipatti, *Mater. Sci. Semicond. Process.* **2017**, *67*, 46.

[94] H. Matsumura, H. Umemoto, A. Masuda, *J. Non-Cryst. Solids* **2004**, *338-340*, 19.

[95] J. S. Orcutt, S. D. Tang, S. Kramer, K. Mehta, H. Li, V. Stojanović, R. J. Ram, *Opt. Express* **2012**, *20*, 7243.

[96] D. Kwong, J. Covey, A. Hosseini, Y. Zhang, X. Xu, R. T. Chen, *Opt. Express* **2012**, *20*, 21722.

[97] S. Zhu, G. Q. Lo, J. D. Ye, D. L. Kwong, *IEEE Photonics Technol. Lett.* **2010**, *22*, 480.

[98] L. Liao, D. R. Lim, A. M. Agarwal, X. Duan, K. K. Lee, L. C. Kimerling, *J. Electron. Mater.* **2000**, *29*, 1380.

[99] A. G. Cullis, *Rep. Prog. Phys.* **1985**, *48*, 1155.

[100] A. T. Voutsas, *Appl. Surf. Sci.* **2003**, *208-209*, 250.

[101] G. Martinez-Jimenez, Y. Franz, A. F. J. Runge, M. Ceschia, N. Healy, S. Z. Oo, A. Tarazona, H. M. H. Chong, A. C. Peacock, S. Mailis, *Opt. Mater. Express* **2019**, *9*, 2573.

[102] Z. Liu, X. Hao, J. Huang, A. Ho-Baillie, M. A. Green, *ACS Appl. Energy Mater.* **2018**, *1*, 1893.

[103] K. Kitahara, K. Shibutani, Y. Okabe, T. Meguro, A. Hara, *Jpn. J. Appl. Phys.* **2015**, *54*, 021302.

[104] L. Wang, W. Wang, Q. Zhou, J. Pan, Z. Zhang, E. S. Tok, Y.-C. Yeo, *J. Appl. Phys.* **2015**, *118*, 025701.

[105] K. Moto, R. Matsumura, T. Sadoh, H. Ikenoue, M. Miyao, *Appl. Phys. Lett.* **2016**, *108*, 262105.

[106] K. Kitahara, Y. Ohashi, Y. Katoh, A. Hara, N. Sasaki, *J. Appl. Phys.* **2004**, *95*, 7850.

[107] S. Nagatomo, Y. Ishikawa, S. Hoshino, *J. Vac. Sci. Technol. B* **2017**, *35*, 051206.

[108] K. Gao, S. Prucnal, R. Huebner, C. Baehtz, I. Skorupa, Y. Wang, W. Skorupa, M. Helm, S. Zhou, *Appl. Phys. Lett.* **2014**, *105*, 042107.

[109] T. T. Tran, D. Pastor, H. H. Gandhi, L. A. Smillie, A. J. Akey, M. J. Aziz, J. S. Williams, *J. Appl. Phys.* **2016**, *119*, 183102.

[110] J. F. Michaud, R. Rogel, T. Mohammed-Brahim, M. Sarret, *J. Non-Cryst. Solids* **2006**, *352*, 998.

[111] H. Byun, J. Bok, K. Cho, K. Cho, H. Choi, J. Choi, S. Choi, S. Han, S. Hong, S. Hyun, T. J. Jeong, H.-C. Ji, I.-S. Joe, B. Kim, D. Kim, J. Kim, J.-K. Kim, K. Kim, S.-G. Kim, D. Kong, B. Kuh, H. Kwon, B. Lee, H. Lee, K. Lee, S. Lee, K. Na, J. Nam, A. Nejadmalayeri, Y. Park, S. Parmar, J. Pyo, D. Shin, J. Shin, Y.-H. Shin, S.-D. Suh, H. Yoon, Y. Park, J. Choi, K.-H. Ha, G. Jeong, *Photonics Res.* **2014**, *2*, A25.

[112] S.-C. Hung, S.-J. Lin, J.-J. Chao, C.-F. Lin, *J. Lightwave Technol.* **2013**, *31*, 3368.

[113] S.-C. Hung, S.-J. Lin, J.-J. Chao, C.-Y. Chang, M.-J. Lin, C.-F. Lin, *J. Lightwave Technol.* **2017**, *35*, 2266.

[114] O. Aktas, S. J. MacFarquar, S. Z. Oo, A. Tarazona, H. M. H. Chong, A. C. Peacock, *Opt. Express* **2020**, *28*, 29192.

[115] Y. H. D. Lee, M. O. Thompson, M. Lipson, *Opt. Express* **2013**, *21*, 26688.

[116] Y. Franz, A. F. J. Runge, S. Z. Oo, G. Jimenez-Martinez, N. Healy, A. Khokhar, A. Tarazona, H. M. H. Chong, S. Mailis, A. C. Peacock, *Opt. Express* **2019**, *27*, 4462.

[117] C.-H. Chou, I-C. Lee, P.-Y. Yang, M.-J. Hu, C.-L. Wang, C.-Y. Wu, Y.-S. Chien, K.-Y. Wang, H.-C. Cheng, *Appl. Phys. Lett.* **2013**, *103*, 053515.

[118] T. Sadoh, M. Kurosawa, A. Heya, N. Matsuo, M. Miyao, *Mater. Sci. Semicond. Process.* **2017**, *70*, 8.

[119] N. Sasaki, M. Arif , Y. Uraoka, J. Gotoh, S. Sugimoto, *Crystals* **2020**, *10*, 405.

[120] J. Schmidtchen, B. Schüppert, K. Petermann, *J. Lightwave Technol.* **1994**, *12*, 842.

[121] J. Schmidtchen, B. Schüppert, A. Splett, K. Petermann, *IEEE Photonics Technol. Lett.* **1992**, *4*, 875.

[122] Y. Chang, S. Y. Chou, J. Kramer, T. W. Sigmon, A. F. Marshall, K. H. Weiner, *Appl. Phys. Lett.* **1991**, *58*, 2150.

[123] S. Stefanov, J. C. Conde, A. Benedetti, C. Serra, J. Werner, M. Oehme, J. Schulze, D. Buca, B. Holländer, S. Mantl, S. Chiussi, *Appl. Phys. Lett.* **2012**, *100*, 104101.

[124] S. Stefanov, J. C. Conde, A. Benedetti, C. Serra, J. Werner, *Appl. Phys. Lett.* **2012**, *100*, 204102.

[125] K. Huet, F. Mazzamuto, T. Tabata, I. Toqué-Tresonne, Y. Mori, *Mater. Sci. Semicond. Process.* **2017**, *62*, 92.

[126] M. J. Aziz, *Metall. Mater. Trans. A* **1996**, *27A*, 671.

[127] T. T. Tran, Q. Hudspeth, Y. Liu, L. A. Smillie, B. Wang, R. A. Bruce, J. Mathews, J. M. Warrender, J. S. Williams, *Mater. Sci. Eng. B* **2020**, *262*, 114702.

[128] J. J. Dubowski, *Proc. SPIE* **2000**, *4048*, 55.

[129] J. J. Dubowski, N. Rowell, G. C. Aers, H. Lafontaine, D. C. Houghton, *Appl. Phys. Lett.* **1999**, *74*, 1948.

[130] M. Weizman, N. H. Nickel, I. Sieber, B. Yan, *J. Non-Cryst. Solids* **2006**, *352*, 1259.

[131] K. Hirose, M. Kobata, T. Sato, K. Kitahara, A. Hara, *Jpn. J. Appl. Phys.* **2010**, *49*, 03CA07.

[132] X. Yang, K. Fujiwara, N. V. Abrosimov, R. Gotoh, J. Nozawa, H. Koizumi, A. Kwasniewski, S. Uda, *Appl. Phys. Lett.* **2012**, *100*, 141601.

[133] C. Y. Ong, K. L. Pey, X. Li, X. C. Wang, C. M. Ng, L. Chan, *Appl. Phys. Lett.* **2008**, *93*, 041112.

[134] L. Dagault, P. Acosta-Alba, S. Kerdilès, J. P. Barnes, J. M. Hartmann, P. Gergaud, T. T. Nguyen, A. Grenier, A. M. Papon, N. Bernier, V. Delaye, J. Aubin, F. Cristiano, *ECS J. Solid State Sci. Technol.* **2019**, *8*, P202.

[135] L. Dagault, S. Kerdilès, P. A. Alba, J.-M. Hartmann, J.-P. Barnes, P. Gergaud, E. Scheid, F. Cristiano, *Appl. Surf. Sci.* **2020**, *527*, 146752.

[136] O. Aktas, S. Z. Oo, S. J. MacFarquar, V. Mittal, H. M. H. Chong, A. C. Peacock, *ACS Appl. Mater. Interfaces* **2020**, *12*, 9457.

[137] M. Brun, P. Labeye, G. Grand, J.-M. Hartmann, F. Boulila, M. Carras, S. Nicoletti, *Opt. Express* **2014**, *22*, 508.

[138] S. Serna, V. Vakarin, J.-M. Ramirez, J. Frigerio, A. Ballabio, X. Le Roux, L. Vivien, G. Isella, E. Cassan, N. Dubreuil, D. Marris-Morini, *Sci. Rep.* **2017**, *7*, 14692.

[139] J. M Ramirez, Q. Liu, V. Vakarin, J. Frigerio, A. Ballabio, X. Le Roux, D. Bouville, L. Vivien, G. Isela, D. Marris-Morini, *Opt. Express* **2018**, *26*, 870.

[140] V. Biryukova, G. J. Sharp, C. Klitis, M. Sorel, *Opt. Express* **2020**, *28*, 11156.

[141] X. Chen, M. M. Milosevic, D. J. Thomson, A. Z. Khokhar, Y. Franz, A. F. J. Runge, S. Mailis, A. C. Peacock, G. T. Reed, *Photonics Res.* **2017**, *5*, 578.

[142] J. E. Cunningham, I. Shubin, X. Zheng, T. Pinguet, A. Mekis, Y. Luo, H. Thacker, G. Li, J. Yao, K. Raj, A. V. Krishnamoorthy, *Opt. Express* **2010**, *18*, 19055.

[143] Q. Xu, S. Manipatruni, B. Schmidt, J. Shakya, M. Lipson, *Opt. Express* **2007**, *15*, 430.

[144] T. Guo, M. Zhang, Y. Yin, D. Dai, *IEEE Photonics Technol. Lett.* **2017**, *29*, 419.

[145] T. Lipka, M. Kiepsch, H. K. Trieu, J. Müller, *Opt. Express* **2014**, *22*, 12122.

[146] B. Chen, X. Yu, X. Chen, M. M. Milosevic, D. J. Thomson, A. Z. Khokhar, S. Saito, O. L. Muskens, G. T. Reed, *Opt. Express* **2018**, *26*, 24953.

[147] R. Loiacono, G. T. Reed, G. Z. Mashanovich, R. Gwilliam, S. J. Henley, Y. Hu, R. Feldesh, R. Jones, *Opt. Express* **2011**, *19*, 10728.

[148] M. M. Milosevic, X. Chen, X. Yu, N. J. Dinsdale, O. Aktas, S. Z. Oo, A. Z. Khokhar, D. J. Thomson, O. L. Muskens, H. M. H. Chong, A. C. Peacock, S. Saito, G. T. Reed, *J. Lightwave Technol.* **2020**, *38*, 1865.

[149] R. Topley, G. Martinez-Jimenez, L. O'Faolain, N. Healy, S. Mailis, D. J. Thomson, F. Y. Gardes, A. C. Peacock, D. N. R. Payne, G. Z. Mashanovich, G. T. Reed, *J. Lightwave Technol.* **2014**, *32*, 2248.

[150] X. Chen, M. M. Milosevic, A. F. J. Runge, X. Yu, A. Z. Khokhar, S. Mailis, D. J. Thomson, A. C. Peacock, S. Saito, G. T. Reed, *Opt. Express* **2020**, *28*, 17630.

[151] I. Staude, J. Schilling, *Nat. Photonics* **2017**, *11*, 274.

[152] L. Wang, M. Eliceiri, Y. Deng, Y. Rho, W. Shou, H. Pan, J. Yao, C. P. Grigoropoulos, *Adv. Funct. Mater.* **2020**, *30*, 1910784.

[153] J. Bonse, S. Höhm, S. V. Kirner, A. Rosenfeld, J. Krüger, *IEEE J. Sel. Top. Quantum Electron.* **2017**, *23*, 9000615.

[154] J. Bonse, S. Gräf, *Laser Photonics Rev.* **2020**, *14*, 2000215.

[155] S. Kaneko, T. Ito, K. Akiyama, M. Yasui, C. Kato, S. Tanaka, Y. Hirabayashi, A. Mastuno, T. Nire, H. Funakubo, M. Yoshimoto, *Nanotechnology* **2011**, *22*, 175307.

[156] D. Qi, X. Li, P. Wang, S. Chen, W. Huang, C. Li, K. Huang, H. Lai, *IEEE Photonics J.* **2014**, *6*, 2200005.

[157] M. Weizman, N. H. Nickel, I. Sieber, B. Yan, *J. Appl. Phys.* **2008**, *103*, 093536.

[158] O. Tokel, A. Turnalı, G. Makey, P. Elahi, T. Çolakoğlu, E. Ergeçen, Ö. Yavuz, R. Hübner, M. Z. Borra, I. Pavlov, A. Bek, R. Turan, D. K. Kesim, S. Tozburun, S. Ilday, F. Ö. Ilday, *Nat. Photon.* **2017**, *11*, 639.

[159] A. Turnali, M. Han, O. Tokel, *J. Opt. Soc. Am. B* **2019**, *36*, 966.

[160] J. Zheng, Z. Liu, C. Xue, C. Li, Y. Zuo, B. Cheng, Q. Wang, *J. Semicond.* **2018**, *39*, 061006.

[161] D. Rainko, Z. Ikonic, A. Elbaz, N. von den Driesch, D. Stange, E. Herth, P. Boucaud, M. El Kurdi, D. Grützmacher, Dan Buca, *Sci. Rep.* **2019**, *9*, 259.

[162] O. Aktas, Y. Yamamoto, M. Kaynak, A. C. Peacock, (*Preprint*) *Research Square*, https://doi.org/10.21203/rs.3.rs-81573/v1, v1, submitted: Nov, **2020**.

[163] L. Yang, J. Wei, Z. Ma, P. Song, J. Ma, Y. Zhao, Z. Huang, M. Zhang, F. Yang, X. Wang, *Nanomaterials* **2019**, *9*, 1789.

[164] K. Sugioka, *Nanophotonics* **2017**, *6*, 393.

[165] M. Malinauskas, A. Žukauskas, S. Hasegawa, Y. Hayasaki, V. Mizeikis, R. Buividas, S. Juodkazis, *Light: Sci. Appl.* **2016**, *5*, e16133.

[166] M. Ams, G. D. Marshall, P. Dekker, J. A. Piper, M. J. Withford, *Laser & Photon. Rev.* **2009**, *3*, 535.

[167] K. Sugioka, Y. Cheng, *Light: Sci. Appl.* **2014**, *3*, e149.

[168] Y. C. Shin, B. Wu, S. Lei, G. J. Cheng, Y. L. Yao, *J. Manuf. Sci. Eng.* **2020**, *142*, 110818.

[169] V. P. Godbole, S. M. Chauhari, *Bull. Mater. Sci.* **1988**, *11*, 97.

[170] S. Wilson, C. Varker, W. Paulson, *IEEE Trans. Nucl. Sci.* **1981**, *28*, 1754.

[171] G. Foti, E. Rimini, in *Laser Annealing of Semiconductors*, (Eds: J. M. Poate, J. W. Mayer), Elsevier, 1982, Ch. 7.

[172] C. Monat, Y. Su, *APL Photonics* **2020**, *5*, 020402.

Biographies and photographs of authors

Ozan Aktas received the B.Sc. degree in electrical and electronics engineering from the Ankara University, Turkey, in 2005, and the M.Sc. and Ph.D. degrees in physics from Bilkent University, Turkey, in 2008 and 2014, respectively. He is a postdoctoral research fellow within the Optoelectronics Research Centre at the University of Southampton, Southampton, U.K. He is currently interested in semiconductor core glass-clad fibers for nonlinear optic applications, and laser processing of semiconductor materials on planar platforms for photonic and optoelectronic applications.

Anna C. Peacock received the B.Sc. and M.Sc. degrees in physics from the University of Auckland, New Zealand, in 1999 and 2001, respectively, and the Ph.D. degree from Optoelectronics Research Centre (ORC), University of Southampton, Southampton, U.K., in 2004. In 2007, she received a five-year Royal Academy of Engineering Research Fellowship, following which she established the Nonlinear Semiconductor Photonics Group. Anna is

currently a Professor in photonics within the ORC, where her interests include the design, development and nonlinear characterization of novel semiconductor waveguides.

Table of contents (ToC) text and figure

Laser Thermal Processing of Group IV Semiconductors for Integrated Photonic Systems

Ozan Aktas and Anna C. Peacock*

This review focuses on laser processing of group IV elemental and compound semiconductors via thermal effects induced by CW and pulsed lasers, which have been used to enhance or tailor the material, structural, electrical, and optical properties. Applications of laser thermal processing are highlighted in fabrication of photonic systems integrated within fiber and planar platforms, presenting challenges and opportunities.

(59 words)